

# The experimental ~~Experimental~~ characterisation of dynamic stall of the FFA-W3-211 wind turbine airfoil

Simone Chellini<sup>1</sup>, Delphine De Tavernier<sup>1</sup>, and Dominic von Terzi<sup>1</sup>

<sup>1</sup>Faculty of Aerospace Engineering, Delft University of Technology, 2629HS Delft, The Netherlands

**Correspondence:** Simone Chellini (s.chellini@tudelft.nl)

**Abstract.** In this work, an experimental campaign was carried out to determine ~~for the first time~~ both the static and dynamic aerodynamic properties of the FFA-W3-211 airfoil. This airfoil is widely used in the wind energy community as part of IEA reference wind turbine designs, but is lacking experimental data for design, simulation tool validation and dynamic stall modelling purposes. The airfoil model was designed and manufactured ~~to be tested for testing~~ in the Low Speed, Low Turbulence wind tunnel ~~of the at~~ TU Delft. The airfoil was tested statically for Reynolds numbers ~~ranging~~ from  $Re_c = 5 \times 10^5$  to  $Re_c = 3.5 \times 10^6$  and dynamically for up to  $Re_c = 2 \times 10^6$ , ~~covering the encompassing~~ steady, unsteady and highly unsteady aerodynamic behaviour. Data were acquired through pressure measurements at the surface of the airfoil and in the wake, as well as by ~~the use of using~~ thermal cameras. The static results ~~highlight highlighted~~ a strong dependence of the lift and drag polars on the Reynolds number and ~~indicate the a change in trends around~~  $Re_c = 2 \times 10^6$ . ~~The suspected~~ presence of laminar separation bubbles for the ~~lowest static Reynolds number regimes. Therefore, two distinct regimes can be identified for the static data between which a~~ ~~lower Reynolds numbers could explain this~~ fundamental change in flow behaviour ~~is observed~~. The dynamic behaviour was studied ~~for the positive, negative and linear regions at high positive angles of attack, high negative angles of attack and within the linear region~~ of the polar ~~around the zero-lift angle~~. The positive region is governed by the lack of a leading-edge vortex. This is in contrast to the negative region of the polars where the effects of a vortex ~~appearing~~ close to the leading edge dominate. The sensitivity of ~~the~~ results to reduced frequency, amplitude, and Reynolds number is discussed. ~~Overall, for the FFA-W3-211 airfoil, it is recommended to use experimental data of~~  $Re_c = 2 \times 10^6$  ~~or above to capture the correct physical (static and dynamic) trends relevant for larger wind turbine blades. For dynamic stall model tuning, it may also be important to consider the significant change in behavior between positive and negative stall angles.~~

## 1 Introduction

Wind turbines have seen a ~~tremendous substantial~~ increase in rotor diameters, as testified in the latest available reference wind turbine (RWT) of the International Energy Agency (IEA), the *IEA 22MW RWT*, which features a rotor diameter of  $D = 284m$  and a hub height of  $h = 170m$  (Zahle et al., 2024). Such a large wind turbine is prone to experiencing significant time-varying inflow conditions along the blades due ~~to~~, among others, ~~to~~ wind shear, turbulence, aeroelastic deflections and yaw misalignment. The force enhancement due to dynamic oscillations is responsible for design loading conditions that are often difficult to quantify and affect the blade's lifespan and overall turbine performance. ~~This is the reason why airfoils that~~

~~undergo dynamic stall effects have generated renewed research interest. The IEA 22MW RWT and its predecessor, the IEA 15MW RWT (Gaertner et al., 2020), employ airfoils from the FFA family at the outboard sections of their blades with different thicknesses depending on their span location.~~ For a given wind condition, dynamic stall ~~is assumed to can~~ be one of the largest sources of load uncertainty for ~~these such~~ wind turbines. This is corroborated by observations that, in simulations of large  
30 rotors, the choice of the dynamic stall model and its airfoil-dependent parameters can lead to qualitatively very different loads  
assessments (see Stettner et al., 2016, for example). For this reason, airfoils that undergo dynamic stall effects have generated  
renewed research interest.

Dynamic stall has long been observed as design driving in applications and, therefore, has been often discussed in the literature, see Ham (1967), Leishman (2002), Gardner et al. (2023) and the citations therein to name only a few. While it is  
35 important to bear in mind that the mechanisms of dynamic stall vary depending on the airfoil profile and flow conditions, a generalisation of the phenomenon could be described as in the following: The boundary layer separation on the airfoil is delayed above the equivalent static stall angle, after which a *dynamic stall vortex* (DSV) is shed from the airfoil's suction side. This process causes a temporary increase in lift exceeding the maximum steady-state equivalent. A nose-down pitching moment and boundary layer reattachment complete the cycle that forms a dynamic stall hysteresis loop. The loop varies greatly  
40 in magnitude depending on the oscillating conditions.

Many experiments have investigated different aspects of dynamic stall, including the effect of add-ons. In De Tavernier et al. (2021), the effect of vortex generators (VGs) ~~effects have been was~~ demonstrated in unsteady conditions for the DU17DBD25, an airfoil specifically designed for a sub-MegaWatt vertical-axis wind turbine. The results were acquired for a chord-based Reynolds number of  $Re = 10^6$   $Re_c = 10^6$ , showing that wind turbine blades would benefit from passive VGs installations  
45 for flow control. In Rainbird et al. (2015), the effects of virtual camber ~~have been were~~ investigated experimentally for the symmetric NACA0018 airfoil. The experimental campaign was carried out in the Parkinson ~~blockage-tolerant~~ blockage tolerant tunnel at Imperial College for  $Re = 3 \times 10^5$   $Re_c = 3 \times 10^5$ . The polars were compared with a CFD study to highlight that consideration of the airfoil's curvature should be included when comparing results from BEM codes with CFD. The NACA 23012 was tested dynamically at  $Re = 1.5 \times 10^6$   $Re_c = 1.5 \times 10^6$  in Leishman (1990). The experiment was carried out in the  
50 Handley-Page low-speed wind tunnel at the University of Glasgow, where data for the  $c = 0.55m$  wing was acquired via 30 pressure taps, highlighting the increasing stall abruptness with increasing Reynolds numbers and the characteristic lift increase associated with the nose-up motion.

Experimental characterisation of the dynamic stall phenomena can be challenging, particularly when combining medium-to-high Reynolds numbers with unsteady reduced frequencies. In the work of Carta (1974) and McAlister et al. (1978), dynamic  
55 stall was analysed for an airfoil pitching sinusoidally. While simplified, the sinusoidal case provides a good testing benchmark replicating helicopter or wind turbine blades. Patterson and Lorber (1990) compared the results of a medium-level Reynolds number experiment carried out for  $2 \times 10^6 < Re < 4 \times 10^6$  for a supercritical airfoil, the *Sikorsky SSC - A09* with two computational methods. The review in McCroskey (1982) provides background for airfoils undergoing transonic flow conditions dynamically.

60 The DNW-HDG facility is used in Llorente et al. (2014) to compare the aerodynamic performance of two wind turbine  
dedicated airfoils. Two wind tunnel experiments were carried out: a high Reynolds test in the DNW-HDG and a medium  
Reynolds in the TU Delft. The campaigns allowed testing across a wide range of Reynolds numbers, from three million up to  
12 million, with varying turbulence intensity. The airfoils tested were the DU 08-W-180, the DU 91-W2-250 and the AWA18-1.  
65 In both experiments, data was acquired through pressure taps distributed on the airfoil surface. The airfoils were extensively  
tested for static angles of attack, highlighting the higher lift obtained for higher Reynolds for the same angles of attack as well as  
static stall delay. Results from the pressurized and non-pressurized facilities were compared for the same airfoil and Reynolds  
number, three million. Importantly, the Mach number associated with the two facilities varies significantly for the same  
Reynolds: this is found to be 0.03 for the Göttingen HDG and 0.23 for the Delft LFT. Despite the geometry and compressibility  
differences, results show a good agreement for the static polars obtained in these two facilities. In Ceyhan et al. (2016),  
70 measurements on a DU 00-W-212 airfoil are presented, which have been taken in the pressurized DNW-HDG wind tunnel  
up to a Reynolds number of 15 million. The high-Reynolds results show a flattening in the aerodynamic efficiency of the wing  
profile. Recently, dynamic stall was studied for a NACA0021 airfoil in Kiefer et al. (2022) ~~for high Reynolds numbers~~ at high  
Reynolds number flows. The experiment was conducted in a pressurised facility where high Reynolds numbers close to ~~the  
real-life condition~~ full-scale conditions can be reproduced. Thanks to a low free-stream velocity, the facility allows the pure  
75 effects of the Reynolds number to be isolated, with no transonic effects due to the low Mach number. Overall, combining  
high Reynolds numbers with dynamic stall testing was proven to be difficult. The literature has repeatedly shown the need for a  
deeper understanding of Reynolds numbers effects for wind turbine airfoils, with a special focus on the more complex transient  
case, which heavily impacts the wind turbine design (Kiefer et al., 2022).

Dynamic stall has been thoroughly investigated ~~via~~ through simulations in the past, often trading off the Reynolds num-  
80 ber and reduced frequency. The work of Boye and Xie (2022) investigates the effects of high reduced frequencies for a  
NACA0012 airfoil, albeit for chord-based Reynolds numbers of only  $Re = 135.000$   $Re_c = 135.000$ . More studies were ~~carried  
out~~ conducted to analyse the pitching of the NACA0012, all for low Reynolds numbers in Tuncer et al. (1990), Choudhuri and  
Knight (1996) and Gharali and Johnson (2013). While the airfoil is often considered a wind turbine benchmark, the low thick-  
ness and lack of a cambered profile make it unsuitable for wind turbines. Gardner et al. (2023) recently highlighted the renewed  
85 interest in dynamic stall, reviewing relevant work in the field. The authors provide an extensive overview of the experimental  
state-of-the-art, as well as future research directions and integration with computational studies. The review highlights the need  
for experiments replicating real-life conditions, both for rotor and fixed-wing aerodynamics. Time-resolved force and pressure  
data are required to fully understand the full temporal analysis of the phenomena. Considerations regarding transition, reverse  
flow and dynamic stall control are also introduced, reviewing passive and active dynamic stall control devices. The review  
90 shows the impact of separation, blade-vortex interactions and shock-airfoil interactions on safer and more efficient rotating  
wing systems.

Dynamic stall predictions rely on simulation data models, such as the Leishman and Beddoes (1989) model, that are not  
developed specifically for wind-turbine tip-airfoils characterised by a thickness of  $\approx 20\%$  (Boutet et al., 2020) and high cam-  
ber. The importance of the Beddoes-Leishman (BL) model and its correct implementation is shown in Melani et al. (2024),

95 highlighting the ~~experimental data's role~~ role of the experimental data in calibrating dynamic stall models correctly. Initial results from Chellini et al. (2024) show the consistent failure of the Beddoes-Leishman model in capturing the transient aerodynamic behaviour, particularly at negative angles of attack, where most dynamic stall models lack experimental calibrations. For instance, despite being based on symmetric airfoil data, the BL model fails to replicate the experimental separation and load enhancement associated with negative angles of attack. In wind turbines, the model is widely adopted in popular tools  
100 such as OpenFAST, leading to inaccurate load reconstructions ~~at negative regimes (Chellini et al., 2024)~~. (Chellini et al., 2024). Other empirical and semi-empirical models such as the models of Onera (McAlister et al., 1984), Oye (Øye, 1991) and Snel (Snel, 1997) could be calibrated similarly to the BL model requiring the corresponding airfoil data.

The IEA 22MW RWT and its predecessor, the IEA 15MW RWT (Gaertner et al., 2020), employ airfoils from the FFA family at the outboard sections of their blades with different thicknesses depending on their span location, for which the dynamic  
105 stall characteristics are not yet fully established. To understand the physical features of dynamic stall on relevant wind turbine airfoils, this work presents the results of the *FFA-W3-211* airfoil tested in static and dynamic conditions. The experiment ~~is~~ was carried out for a range of static and dynamic inflow angles and steady to highly unsteady reduced frequencies, ~~aiming~~ chosen to characterise three distinct flow regions in the negative, linear and positive regions of the polars.

## 110 1.1 Objective and paper structure

This work presents ~~the first~~ experimental data for the FFA-W3-211 airfoil, quantifying the static and dynamic aerodynamic behaviour. The ~~main~~ primary objective is to ~~determine~~ investigate how the combination of reduced frequency and Reynolds number ~~affects~~ impacts the airfoil's ~~loading~~. ~~The analysis~~ dynamic loading. Analysis is carried out to understand the driving factors affecting the flow physics around the airfoil. Firstly, the ~~corrections~~ experimental post-processing procedure is intro-  
115 duced. This is followed by validating the newly acquired data against existing experimental results in §3.1. The analysis of the static and dynamic loads follows in §3.2. The analysis is divided into Reynolds number, reduced frequency, oscillating frequency and amplitude effects, isolating ~~all~~ the experimental and relevant flow physics parameters.

## 2 Experimental set-up

### 2.1 Wind tunnel facility

120 The experimental campaign is carried out in the *Low-Speed Low-Turbulence wind tunnel* (LTT) of Delft University of Technology, a closed-section recirculating wind tunnel. The facility features changeable octagonal testing sections, with a width of 1.80m, length of 2.60m and height of 1.25m. The octagonal testing section returns a cross-sectional area of  $A_{l_{tt}} = 2.07m^2$ . Each testing section is equipped with a mechanically actuated turntable flush to the tunnel's top and bottom walls, which allows the airfoil's angle of attack to be set with a precision of  $\pm 0.1^\circ$ . The turbulence level varies from 0.015% at  $20m/s$  to  
125 0.07% at  $75m/s$  due to the large contraction ratio of 17.83. The six-bladed fan is powered by a 525 kW DC motor, returning

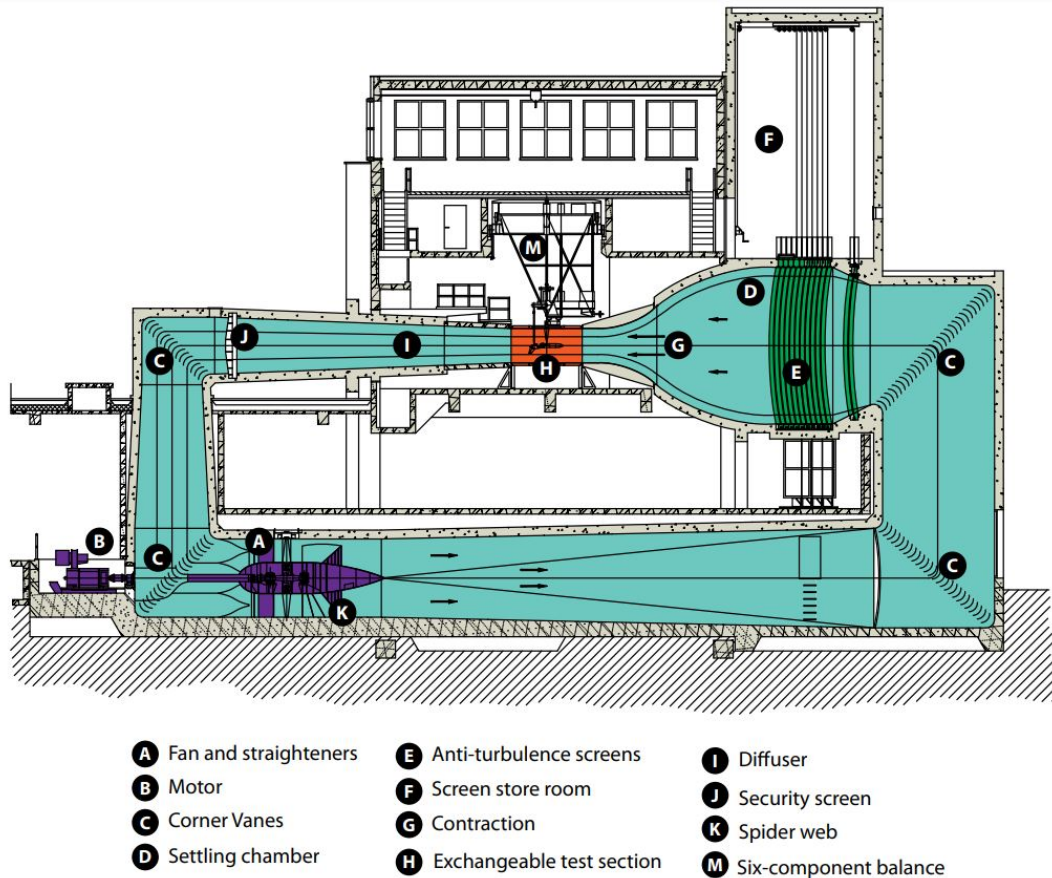


**Figure 1.** Diagram of the low-speed, low-turbulence wind tunnel at TU Delft. The flow reaches the testing section from right to left.

a free-stream velocity up to  $U_\infty = 120\text{ms}^{-1}$ , and Reynolds numbers up to  $Re_c = 3.5 \times 10^6$  based depending on the airfoil's chord can be tested. More details can be found in Delft (2017). The full diagram of the facility can be found in Fig. 1.

## 2.2 Airfoil model

An FFA-W3-211 airfoil model with a maximum thickness of 21.1% chord (Fig. 2) is manufactured from carbon fibre composite. The airfoil model has a chord length of  $c = 600$  mm and a length of  $h = 1246$  mm to span the LTT test-section height, resulting in an aspect ratio  $AR \approx 2$ , in line with previous airfoils tested in this facility (e.g., Baldacchino et al., 2018; Timmer and Van Rooij, 2003; Llorente et al., 2014). The trailing edge thickness is measured as carbon fibre thickness varies along the airfoil's span, with local refinements around the leading edge. Due to the high skin thickness, with a minimum of  $t = 1.7\text{mm}$  and a maximum of  $t = 6\text{mm}$  at the leading edge, no visual surface deformation was observed during the experiment. The trailing edge thickness is measured as 1.7 mm. The airfoil is connected vertically to the wind tunnel's walls through an

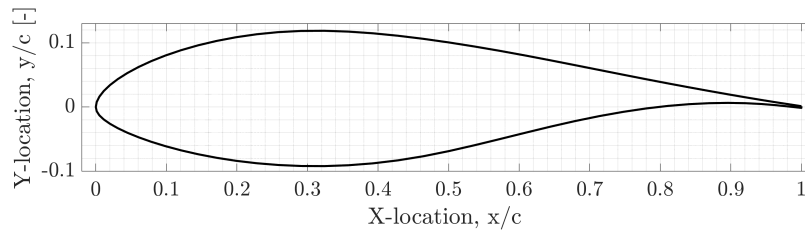


**Figure 2.** Cross section of the FFA-W3-211 airfoil. The cambered airfoil has a thickness of 21.1 %.

aluminium shaft, which exits the wind tunnel on the upper side to be connected to a linear actuator. A metal insert secures the shaft to two outer wooden ribs. The airfoil is fixed by two ball bearings mounted on support plates and two safety pins for a total of four contact points. The plates are inserted inside the wind tunnel turntable rails and secured flush to the testing section-mm.

140 A total of 93 pressure taps, refined around the leading edge, with a diameter of 0.4 mm, are distributed on the airfoil skin. The taps distribution is angled at  $\approx 15^\circ$  to reduce any potential boundary layer disruption between the orifices. Each pressure tap is connected to an  $\approx 2.7$  m long tube, which exits the airfoil model through a lower aperture located at around  $x/c = 0.5$ . Importantly, this represents a limitation for the airfoil's oscillating amplitude, which can operate safely between  $-25^\circ < \alpha < 25^\circ$ . The airfoil model was polished to a mirror-finish texture, and the flow transition from laminar to turbulent was verified with  
 145 thermal cameras to ensure that no model imperfection provoked early transition, as shown in Fig. 3, and prove the confirm sufficient 2D uniformity of the model. A comparison between  $Re_c = 1.0 \times 10^6$  and  $Re_c = 3.5 \times 10^6$  is visible in Fig. 3. At the top of Fig. 3, an irregularity is visible, which is caused by light reflections from the wind tunnel walls and a small defect in the surface (only visible at the higher Reynolds number). Based on the defect being ocated far away from the pressure orifices and by inspecting drag measurements derived from pressure measurements in the wake (not shown in this paper), it was concluded  
 150 that this artifact is unlikely to have influenced any of the measurements reported here.

## 2.3 Data acquisition

### 2.3.1 Static measurements

The 2D flow data was acquired through the 93 pressure taps, connected to the pressure scanner through four adapters. The pressure measurements at the leading and trailing edges were split into two channels for redundancy. The pressure scanner was  
 155 also used to acquire the total and static pressure in the wind tunnel. In static cases, a wake rake is used to quantify the loss of momentum in the wake. This comprises 67 pressure tubes and 16 static tubes over a length of 504 mm. The pressure rake automatically moves in the horizontal direction to centre the centres the wake and traverses along the spanwise direction for each acquisition to average potential three-dimensional flow effects. When the rake can no longer capture the airfoil's turbulent wake, pressure drag is used instead. Data is are sampled at a frequency of 5Hz. Two A 2mm gaps are gap is found between the  
 160 wind tunnel walls and the wing on each side. The gaps were sealed with tape for during the static measurements , minimising

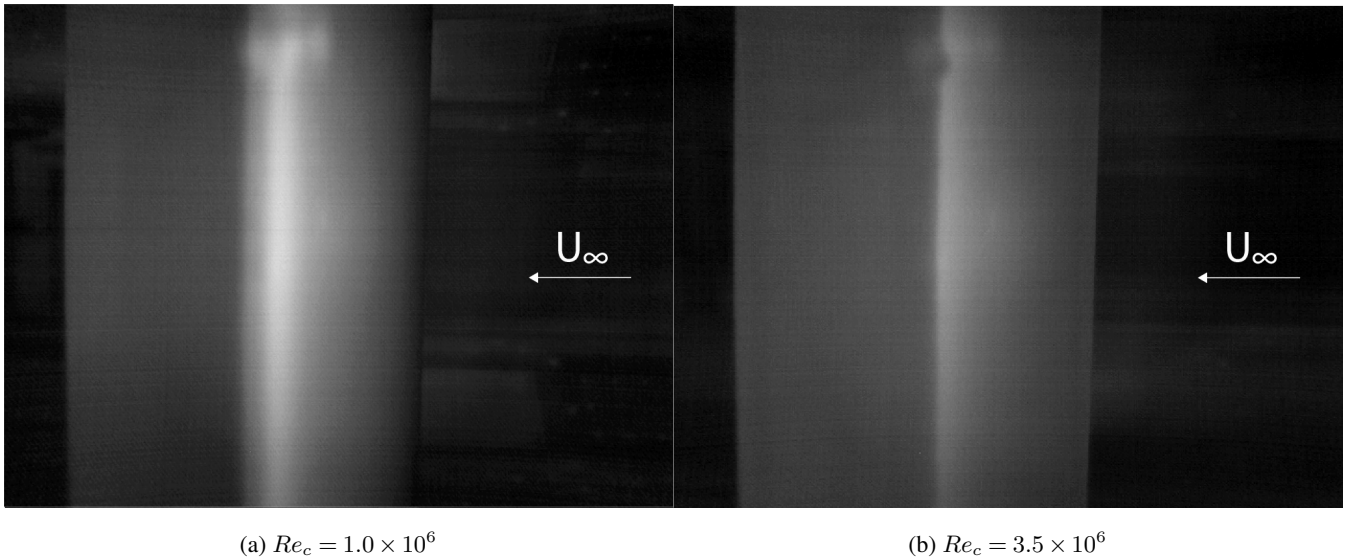


**Figure 3.** Qualitative transition location on the airfoil's suction side for  $\alpha = 0^\circ$ . The upper reflection does not affect the airfoil's wake-derived drag coefficient and surface pressure-derived lift coefficient.

in order to minimise the loss of momentum from the lower aperture, from-through which the pressure tubes exit ~~the model,~~ and the 3D finite wing effects.

The airfoil ~~is rotated through the~~ section is rotated using the wind tunnel turntable for the static polars acquisition around its quarter-chord ~~pointline.~~ The static polars are acquired for angles of attack of  $-20^\circ < \alpha < 20^\circ$ . Local refinements are carried out to characterise the stall region and the design lift-to-drag ratio. The static experiment is carried out for  $5 \times 10^5 < Re_c < 3.5 \times 10^6$ . Therefore, the equivalent Mach number for the highest Reynolds number case is evaluated as  $M = 0.25$ , and compressibility effects ~~are neglected in this analysis.~~ Depending on the boundary layer thickness, Reynolds number and angle of attack, impurities in the boundary layer can disrupt the pressure readings from the can be assumed negligible in the analysis. To avoid any impurities on the airfoil's tap, especially towards the leading edge, voiding part of the dataset. Therefore, the ~~airfoil surface, that may lead to early boundary layer transition, the~~ model was regularly cleaned to ensure a smooth, guarantee a clean dust-free surface and prevent any undesired boundary layer transition.

~~Following the clean airfoil tests, a zigzag tape was applied to the airfoil at  $x/c = 5\%$  on both the suction and pressure sides. Different tape thicknesses were considered to ensure a complete boundary layer transition to turbulence independent of the Reynolds number and angle of attack. Three different zigzag tapes were tested, with a thickness of 0.4, 0.5, 0.65mm to transition the flow at  $x/c = 5\%$  on the pressure and suction side. Transition to turbulence was observed for Reynolds numbers in the range  $5 \times 10^5 < Re_c < 3 \times 10^6$  and for multiple angles of attack. It was decided to employ a 0.4mm zigzag tape to~~

~~trigger transition for all cases with a reduced drag penalty compared to thicker zigzag tapes. The lower and upper pressure distributions~~

180 The lower pressure distribution  $C_{p,l}$  and upper pressure distributions  $C_{p,u}$ , obtained from the pressure taps on the airfoil's surface, are integrated to determine the normal coefficient (Eq. (1)), where the prime indicates, here and in the following, uncorrected values.  $c$  is the airfoil chord.

$$C'_n = \int_0^1 (C_{p,l} - C_{p,u}) d\left(\frac{x}{c}\right) \quad (1)$$

185 ~~Where  $C_{p,l}$  and  $C_{p,u}$  are the lower and upper pressure distributions, respectively.~~ The drag coefficient is obtained through the wake rake ~~as~~ pressure readings according to Eq. (2), where  $C_{p,t}$  is the total pressure and  $C_{p,s}$  refers to the static pressure

$$C'_d = \frac{2}{c} \int_{\text{wake}} \sqrt{C_{p,t} - C_{p,s}} \left(1 - \sqrt{C_{p,t}}\right) dy \quad (2)$$

The normal and drag coefficients and the angle of attack ( $\alpha$ ) are used to quantify the 2D lift in Eq. (3).

$$C'_n = C'_l \cos(\alpha) + C'_d \sin(\alpha) \quad C'_l = \frac{C'_n}{\cos(\alpha)} - C'_d \tan(\alpha) \quad (3)$$

### 2.3.2 Dynamic measurements

190 The wing model's shaft was connected to a UniMotion PNCE 40 BS 1610 linear actuator for dynamic testing purposes. The actuator's extrusion is connected to the airfoil's steel shaft to couple the linear and pitching motions, and its extrusion is controlled through a LabVIEW script. An angular encoder is coupled to the airfoil's shaft, providing the real-time angle of attack reading. More details regarding the setup can be found in De Tavernier et al. (2021). Data is sampled from the wing's pressure taps with the same methodology described in the previous section, with a frequency of  $300\text{Hz}$ . The dynamic polars were  
195 acquired by pitching the airfoil ~~around its quarter-chord point~~ section around its quarter-chord line.

~~Depending on the flow conditions, different actuator calibrations were needed. The increased aerodynamic loads for the clean airfoil configuration shifted the zero angle of attack for the equivalent transitioned flow case. Additionally, relevant calibration differences were observed after the static stall angle and as a consequence of increasing Reynolds numbers. As a representative example, the initial arm position reported a half a millimetre difference between transitioned  $Re_c = 2 \times 10^6$   
200 and clean  $Re_c = 1 \times 10^6$ . This may not seem like a lot; however, translated into an effective angle of attack, this difference is responsible for an offset of  $\pm 0.3^\circ$  for the pitching motion.~~ Due to the aerodynamic loads acting on the airfoil model, airfoil pitching system and its connection, the set-up was experiencing some aeroelastic response. To cope with this, the actuator calibration (linking the actuator motion to the airfoil angle of attack) was performed independently for different Reynolds numbers, to guarantee accurate angles of attack.

205 A representative, yet simplified, oscillation case for a wind turbine airfoil is defined by a simple sinusoidal motion, described in Eq. (4) as

$$\alpha(t) = \alpha_0 + A \sin(2\pi ft), \quad (4)$$

CAD diagram of the wind tunnel section. The turntable walls hold the airfoil in place and rotate for static data acquisition.



**Figure 4.** Experimental setup details. The top left image shows the testing section geometry, with the wake rake behind the ~~taped~~ airfoil. The linear actuator mechanism is shown in the top right image. The testing section installed in the wind tunnel is shown in the bottom left image, without the covering panels ~~on~~ for visibility purposes. The airfoil model ~~taped to~~ (with sealed gaps between the wind tunnel walls and airfoil model) is shown in the bottom right image, with the thermal cameras installed at the airfoil's midspan, for  $x/c = 50\%$

where  $\alpha_0$  is the initial mean angle of attack,  $A$  is the oscillating amplitude, and  $f$  is the oscillating frequency in Hertz. The actuator was controlled through a LabVIEW ~~code, setting the mean angle of attack, oscillating amplitude, frequency and acquisition time. The actuator is secured above the wind tunnel testing section and bolted into the turntable panels.~~ program.

The frequency ~~value~~ from Eq. (4) also ~~affects~~ sets the reduced frequency,  $k$ , which is defined here as Eq. (5):-

$$k = \frac{\pi c f}{U_\infty}, \quad (5)$$

where  $c$  is the airfoil's chord and  $U_\infty$  is the free-stream velocity. This non-dimensional parameter describes the ~~unsteadiness of~~ degree of unsteadiness in oscillation. Three separate unsteady regimes are identified in Corke and Thomas (2015). The flow field can be considered unsteady for  $0.05 \leq k \leq 0.2$ , and highly unsteady for  $k \geq 0.2$ , ~~highly unsteady~~. Below 0.05, the unsteady effects ~~can be neglected~~ may be assumed negligible and, therefore, the corresponding flow regime is commonly

**Table 1.** Dynamic experimental matrix. Each parameter is changed independently of the others, returning four independent degrees of freedom in the experimental matrix.

Reynolds number [f]	Frequency [Hz]	Amplitude [°]	Mean Angle [°]
$Re_c = 5 \times 10^5$	0.6	$\pm 3$	-9.4
$Re_c = 1 \times 10^6$	1.2	$\pm 5$	-1.4
$Re_c = 2 \times 10^6$	1.8	$\pm 7$	9.6
<del>/</del>	2.4	$\pm 9$	<del>/</del>
<del>/</del>	<del>/</del>	$\pm 11$	<del>/</del>

referred to as quasi-steady. To capture the three different unsteady flow regimes, a comprehensive span of Reynolds numbers and reduced frequency is acquired for frequencies is acquired around the negative and positive stall regions and the linear region of the polars. The dynamic matrix is repeated for the clean case and for the transitioned case, using the same zigzag tape described in the previous paragraph.

Together with the local pressure on the airfoil, the atmospheric and operational conditions were recorded through the wind tunnel measurement devices, highlighting a variation in the instantaneous free-stream readings due to the changing blockage in the wind tunnel. Data was acquired starting from the negative mean angle of attack, first acquiring the lowest frequency and amplitude were acquired for 50 loops of dynamic stall sinusoidal cycles.

Finally, low-frequency cases were acquired with the same methodology to determine the reduced frequency at which the dynamic effects disappear for the polars, for which data was acquired at  $30\text{Hz}$ . The experimental matrix is found in Tab. 1, where one parameter at the time was changed.

## 2.4 Measurement corrections

### 2.4.1 Static data corrections

The static raw pressure data is are corrected using the wall effects corrections found in Dalton (1971), correcting wall effects correction approach defined in Dalton (1971). This approach corrects for lift interference, wake blockage, solid blockage, and streamline curvature. Here, the uncorrected drag is used to correct for wake blockage, directly affecting the corrected lift coefficient. At high angles of attack, the turbulent airfoil's wake becomes too wide to be captured by the rake. Depending on the Reynolds number, the wake is moved outside the wake. Therefore, the drag is determined by integrating the pressure distribution along the airfoil surface, which is common practice (De Tavernier et al., 2021). The wake blockage is defined in Eq. (6) as

$$w_b = C_D \frac{0.25h}{c} \frac{1 + 0.4M^2}{\beta^2} \quad (6)$$

~~Where where~~  $M$  is the Mach number, and the compressibility factor  $\beta$  is defined as  $\beta = \sqrt{1 - M^2}$ . The wind tunnel blockage factor,  $\sigma$ , ~~compressibility factor  $\beta$  are defined in Eq. (7): is defined as~~

$$240 \quad \sigma = \frac{\pi^2}{48} \left( \frac{c}{h} \right)^2 \quad (7)$$

The angle of attack is corrected using Eq. (8)

$$\alpha = \alpha' + \frac{57.3\sigma}{2\pi\beta} (C'_l + 4C'_m) \quad (8)$$

#### 2.4.2 Dynamic data corrections

Due to the dynamic oscillations, retrieving ~~the drag coefficient drag~~ readings from the wake rake ~~was impossible. This was due to the large and variable wake shed by the airfoil, which the rake would not fully capture. The became unreliable. As the~~ drag coefficient is used ~~in the static corrections~~ to obtain the lift coefficient, ~~and~~ it is not possible to ~~transition from convert~~ normal and tangential coefficients to the lift coefficient ~~without the drag quantification~~.

An initial delay and amplitude loss are found between the pressure sampled at the skin of the airfoil and ~~the DAQ values at the end of the pressure tubes~~. Considering the pressure tube length, width, and testing conditions, the pressure lag and attenuation ~~can be evaluated are handled~~ in the post-processing using the ~~corrections correction method~~ from Bergh and Tjrdeman (1965). The method ~~has been was~~ coded in the software tool PreMeSys V2.0, validated in De Tavernier et al. (2021) for dynamic airfoil testing. The corrected pressure values are then translated into instantaneous forces on the airfoil by ~~means of~~ integration.

While a methodology concerning aerodynamic ~~static corrections has (static) corrections for the presence of the wind tunnel walls had~~ been validated, evidence of dynamic ~~corrections has wall corrections are~~ yet to be found in the literature. ~~Previous literature~~ ~~Therefore, previous literature~~, such as Kiefer et al. (2022) and De Tavernier et al. (2021) ~~display, displayed~~ the dynamic polars ~~results uncorrected for any of the traditional voices mentioned in the last paragraph. A preliminary study assessed the impact of drag coefficient in the static corrections and validated the corrections from Dalton (1971) for the pitching airfoil ease. in an uncorrected manner. To quantify the potential effect of reporting uncorrected dynamic data rather than corrected dynamic data, Fig. 5a is provided. This figure~~ shows the differences between the corrected, uncorrected and ~~partially corrected results. The lift curve slope is shown a partially corrected static lift polar~~ for  $Re_c = 10^6$ , ~~with corrections from Allen and Vincenti (Dalton, 1971) fully applied, partially applied and uncorrected~~. There is good agreement between the fully and partially corrected data regarding the location and value of  $C_{L_{max}}$  and pre-stall slope. However, after the stall angle is reached, the effects of wake blockage become predominant in the ~~polars~~ corrections, with the partially corrected data diverging from the fully corrected data as the angle of attack increases and accounting for almost 50% at  $\alpha = 20^\circ$ . ~~However, as the correction approach is not proven, it was decided not to correct the data for wall effects and report uncorrected data only.~~

~~The safety pins that block the airfoil to the wind tunnel testing sections were removed to pitch the airfoil around its quarter chord point. Thus~~ ~~When testing dynamically~~, the tape ~~that sealed sealing~~ the 2mm gap between the airfoil walls and the wind

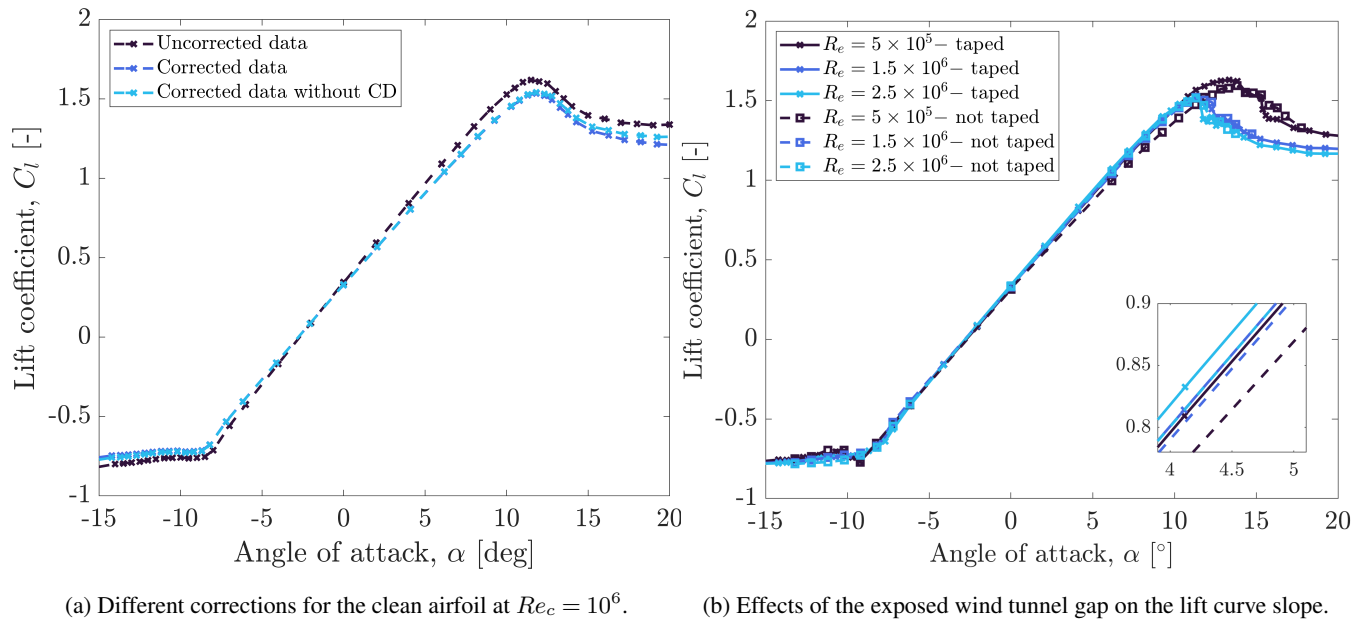


**Figure 5.** Effects of the wake-blockage term and sealed wind-tunnel gap in the static lift coefficient curve

270 tunnel was removed, exposing the. This introduces 3D finite wing effects and allows flow to exit the tunnel through the (small) gap on the lower plate that allows the pressure tubes to exit the model side of the wind tunnel. At low angles of attack, the airfoil cross-section fully or partially covers the gap, limiting the loss of momentum. However, as the angle of attack increases, the gap is more exposed to the free-stream flow. A calibration was carried out ahead of the dynamic acquisitions to assess the The loss of momentum through the wind tunnel aperture was determined for the linear region of polars. The effect of the sealing 275 tape was quantified for three static cases, for  $Re_c = 5 \times 10^5, 1.5 \times 10^6, 2.5 \times 10^6$ , as shown of which one is shown for clarity in Fig. 5b. The linear region slope is reported for To quantify the effect, the linear slope (defined between  $-6^\circ < \alpha < 6^\circ$ ) is reported in Tab. 2. The results show a good agreement in the linear region of the polars for all cases minor effects, with the difference in the pre-stall slope decreasing with increasing Reynolds numbers. This is due to the higher flow inertia that, for higher free-stream velocities, allows the suction of the wind tunnel cavity to be overcome. As the static stall angles are 280 approached, the loss of momentum becomes more evident for low Reynolds numbers while still showing similar stall trends across all cases. While the differences are within a reasonable range, it is believed that no additional correction is needed.

### 3 Results and discussion

#### 3.1 Validation

The static polar results can be are validated against existing experimental data. To the best of the authors' knowledge, the 285 only experimental dataset available concerning the aerodynamic performance of the FFA-W3-211 airfoil is Bertagnolio et al.

**Table 2.** Lift-Variation in lift curve slope calibration in the linear region of the polars due to mass outflow and 3D finite wing effects for different Reynolds numbers. The quantification is not taken into account when reporting the dynamic polars results.

	Sealed gap slope	Open gap slope	Difference
$Re_c = 5 \times 10^5$	0.1177	0.1141	-3.1%
$Re_c = 1.5 \times 10^6$	0.1185	0.1158	-2.3%
$Re_c = 2.5 \times 10^6$	0.1205	0.1183	-1.8%

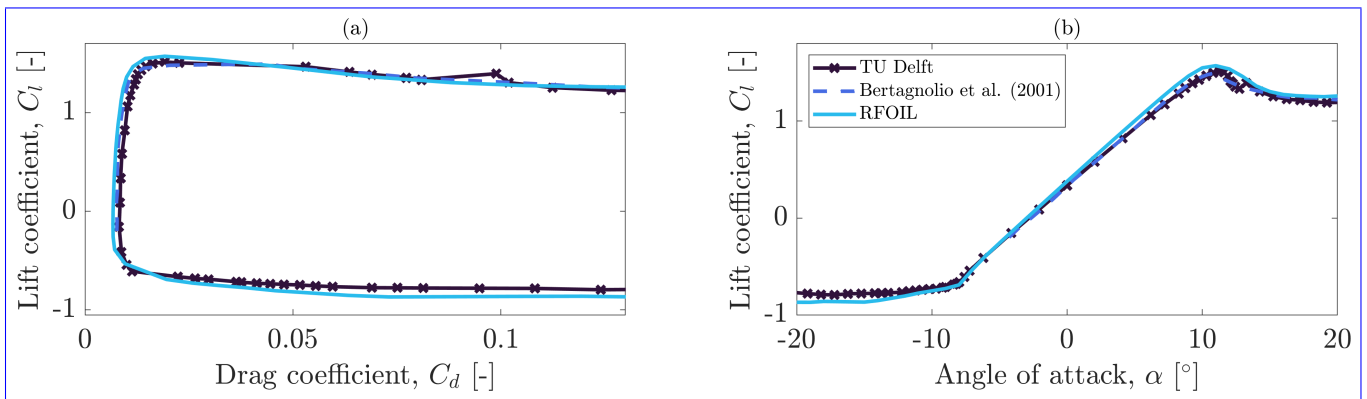


**Figure 6.** Clean polars comparison for the FFA-W3-211 airfoil for  $Re_c = 1.8 \times 10^6$

(2001). In their work, the FFA-W3-211 airfoil was tested for a chord-based Reynolds number of  $Re_c = 1.8 \times 10^6$  in the low-speed wind tunnel L2000 at KTH. The experimental facility has a two by two metres section, with a turbulence intensity of 0.15%. The static polars were acquired for  $-5.43^\circ < \alpha < 31^\circ$ . Finally, results from the compressible panel method from RFOIL simulations are included (Van Rooij, 1996). Results shown-The results depicted in Fig. 6 show good agreement in both the lift and drag coefficients and allow the wind tunnel model and methodology to be considered as validated.

### 3.2 Static polars

The newly acquired airfoil polars are the starting point for this analysis. Static results are presented in Fig. 7. The lift coefficient linear region slope slope in the linear region of the lift coefficient curve slightly increases with the Reynolds number. Here, the-The highest aerodynamic efficiency shows more significant Reynolds number effects. Firstly, the  $(C_l/C_d)_{max}$  increases in magnitude with increasing Reynolds numbers. Secondly, the value of  $\alpha$  at which the highest aerodynamic efficiency is found decreases with increasing Reynolds numbers. The aerodynamic efficiency is found to be heavily dependent. Overall, the aerodynamic efficiency depends strongly on the Reynolds number, as explained in Ceyhan et al. (2017). A regime was identified after  $Re = 2 \times 10^6$ , after which As the Reynolds number increases, the maximum lift coefficient value

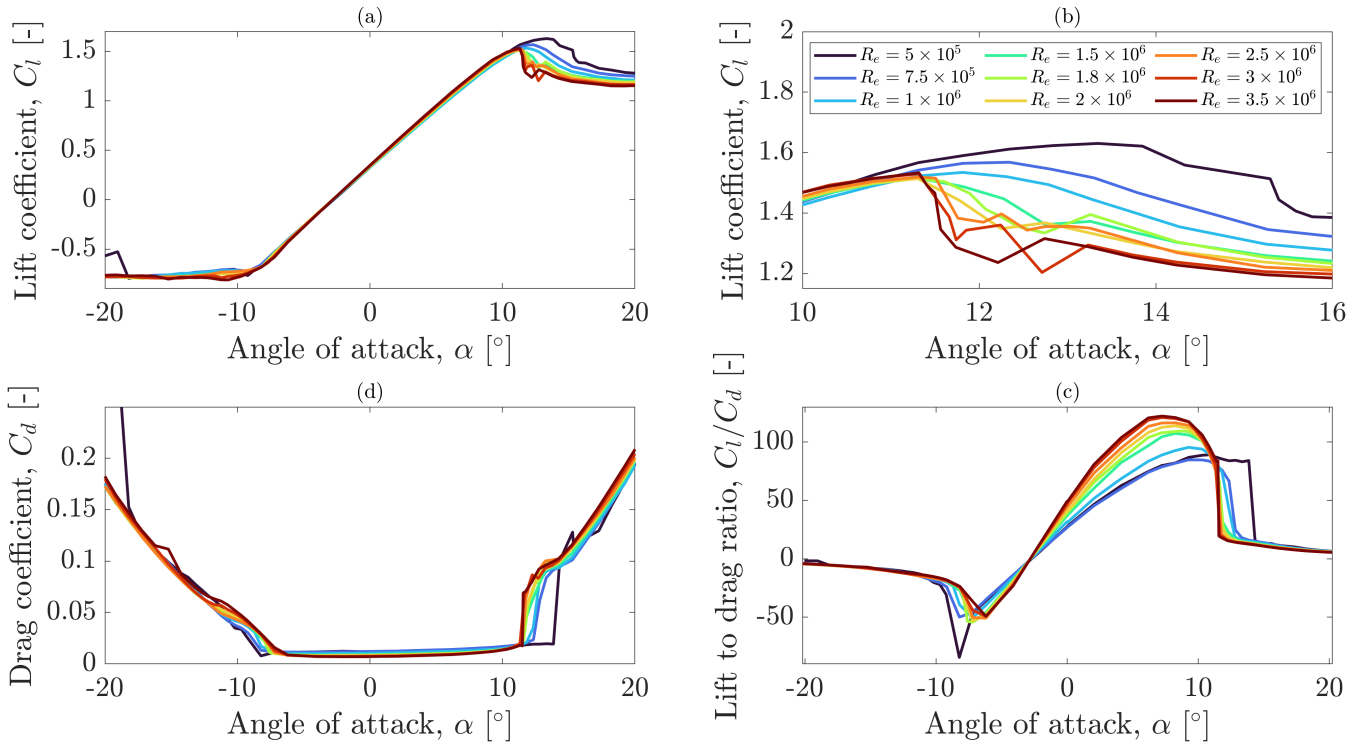


**Figure 7.** Clean static polars for the FFA-W3-211 for  $5 \times 10^5 \leq Re_c \leq 3.5 \times 10^6$ .

increases drops, however above  $Re_c = 2 \times 10^6$ , it increases again. The same regime-kind of regime change was identified in Brunner et al. (2021), highlighting a shift from trailing-edge stall to leading-edge stall for higher Reynolds numbers for a different airfoil. The angle of attack at which the maximum lift coefficient is found follows a similar trend. At low Reynolds numbers, stall occurs at higher angles of attack, which decrease. This angle decreases as the Reynolds number increases due to a combination of different boundary layer thicknesses and separation points. It can be concluded that a different regime is identified, which is solely due to the effects of the as a result of a combination of changes in boundary layer thickness and the separation point, but stays roughly constant after  $Re_c = 2 \times 10^6$ . From the above, we can conclude that two distinct regimes exists that are solely determined by how the polars are impacted by a change in Reynolds number.

The effects of a An explanation for this change in physical behavior could possibly be the presence of a small laminar separation bubble (LSB) can be observed in the pressure distribution for the low Reynolds cases. This is particularly strong for  $Re_c = 5 \times 10^5$ , where the bubble can be observed on both the suction and pressure sides for the lower Reynolds numbers that vanishes at the higher Reynolds numbers (also depending on the angle of attack). An indication for this speculation can be found in Fig. 8 (a). As the Reynolds number increases, the effects of the LSB decrease. The LSB fixes the flow transition to around  $x/c = 30\%$ , decreasing in magnitude as the flow inertia becomes greater. Here, for  $Re_c = 5 \times 10^5$ , a small plateau in the pressure coefficient could be discerned for both the suction and pressure sides at roughly  $0.32 < x/c < 0.40$  and

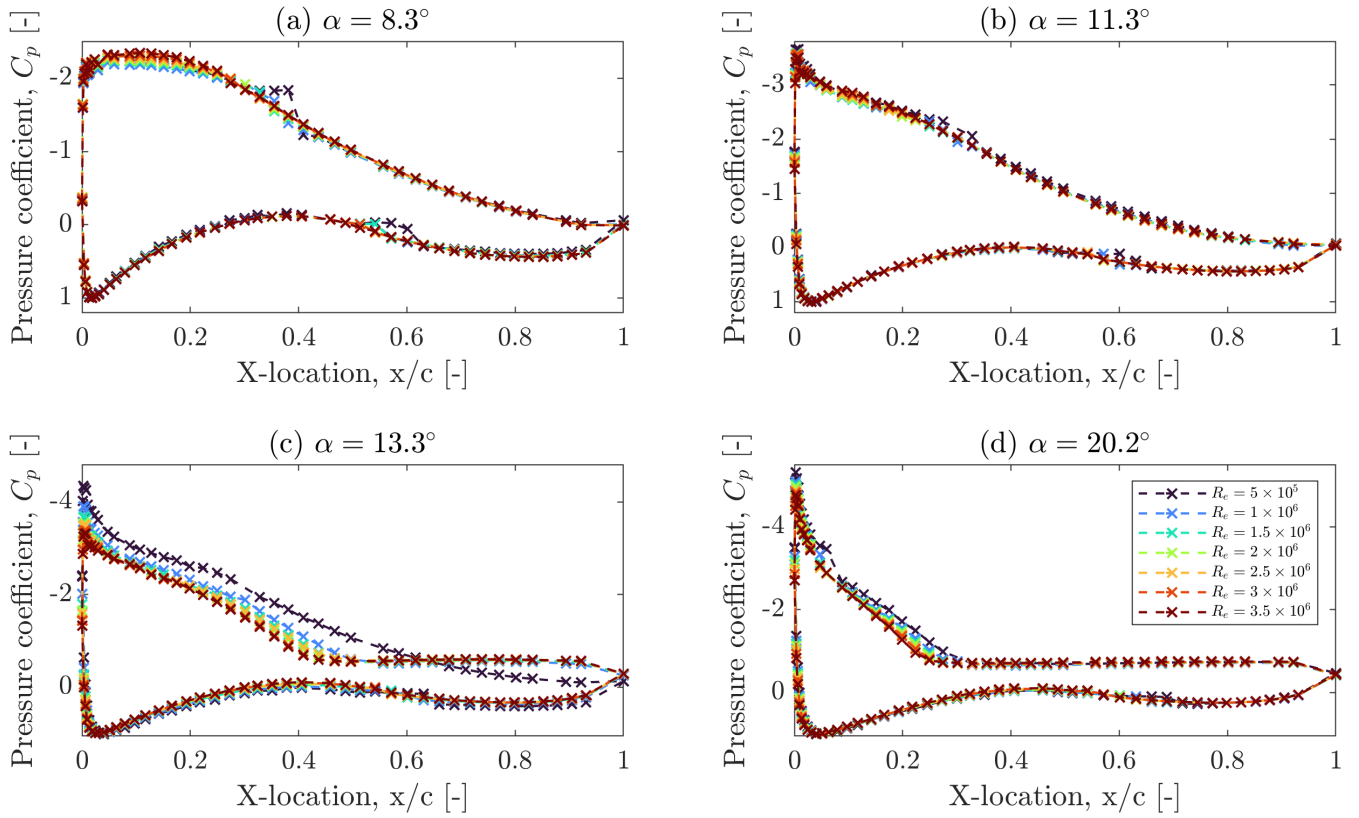


**Figure 8.** Pressure contours for relevant angles of attack.

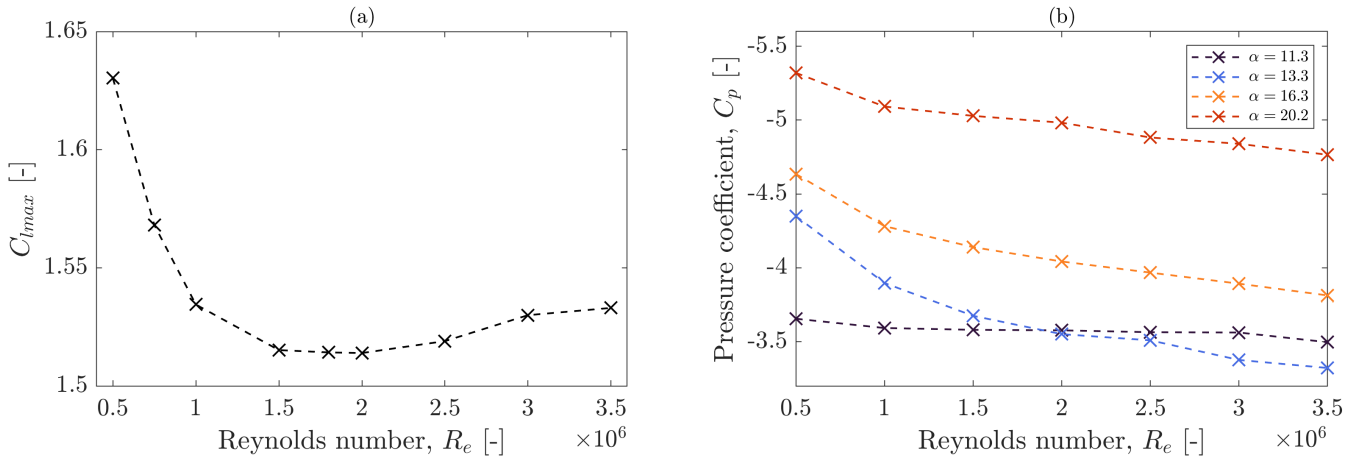


**Figure 9.** Maximum lift coefficient (a) and suction peak (b) as a function of Reynolds number and angle of attack for the clean airfoil.

0.47 <  $x/c$  < 0.65, respectively. An increase in Reynolds number (or angle of attack) can move the location of laminar-to-turbulent transition upstream and thus diminish or eliminate the LSB.

The position and magnitude of the suction peak also change with the Reynolds number. A higher suction peak is first identified for low Reynolds numbers. For the same angle of attack, the  $x/c$  position at the highest magnitude slightly shifts towards the trailing edge for increasing Reynolds numbers. The trend is shown in Fig. 9, where the static stall angle is also presented. Here, the magnitude of the suction peak shows Reynolds number effects.

The different stall behaviour also highlights the effects of the Reynolds number. The stall behaviour is gradual for the regimes in which an LSB is found in suspected from the pressure distribution. The stall becomes more abrupt for the highest Reynolds number, in agreement with high-Reynolds literature. The stall behaviour can be classified as a trailing-edge stall for all the the lowest tested Reynolds numbers and angles of attack. As the Reynolds number increases, the separation point on the suction side moves towards the leading edge. Figure 8e shows (b) shows the change in stall behaviour, from a smooth transition at lower Reynolds regimes to a more abrupt drop. Figure 8 (c) indicates that for  $\alpha = 13.3^\circ$ , the flow is only attached for for the  $Re_c = 5 \times 10^5$  case. Figure 8d shows (d) displays the effects of the Reynolds number on the location of the separation point, which moves upstream with increasing Reynolds numbers. This is associated with a decreasing suction peak magnitude,  $C_{p_{min}}$ , as shown in Fig. 9 (b). Figure 9 a shows the Reynolds effects on the maximum lift coefficient. As shown in Brunner et al. (2021) and Kiefer et al. (2022) for a NACA0021, the maximum lift coefficient value is found to increase past the  $Re_c \approx 2 \times 10^6$  regime. From all of the above, for the FFA-W3-211 airfoil, static experiments of  $Re_c = 2 \times 10^6$  or above are recommended to more likely capture correct physical trends relevant for larger wind turbine blades.

### 3.3 Dynamic polars

Reynolds number sweep for  $f = 1.2Hz$ ,  $A = 7^\circ$ . The reduced frequency range is  $k = 0.182, 0.091, 0.046$ . The full line represents the upstroke airfoil section movement, while the dotted line represents the downstroke movement. Data averaged over 50 dynamic stall cycles.

As previously mentioned, The dynamic results are evaluated by isolating (where possible) Reynolds number effects and the response to different reduced frequencies, oscillating frequencies and amplitudes. Note that capturing the large wake shed by the airfoil with a rake for the dynamic cases was not possible. Therefore, the (uncorrected) normal coefficient results are presented and averaged over 50 loops of dynamic stall for all cases. The results are divided into Reynolds number, reduced frequency, oscillating frequency and amplitude sweeps for easy comparison. The normal coefficient results are angles of attack are presented with an accuracy of  $\pm 1^\circ$  due to some minor play in the linear actuator motion, particularly found for the highest inertia cases.

#### 3.3.1 Reynolds number effects

Results-

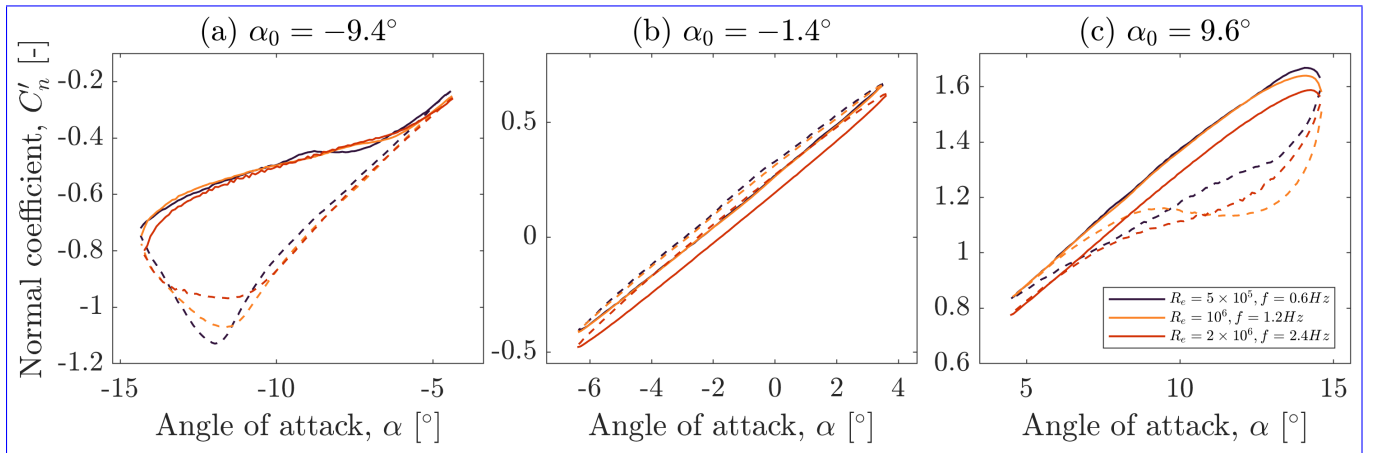


**Figure 10.** Reynolds number effects for a constant value of  $k = 0.091$ . The airfoil section is oscillated with an amplitude of  $\pm 5^\circ$ . The full line represents the upstroke movement, while the dotted line represents the downstroke movement. Data averaged over 50 dynamic stall cycles.

The results shown in Fig. 11 show the isolated Reynolds number effects on the dynamic normal coefficient. Three representative for the same reduced frequency. To obtain a constant value of  $k$  for the tested Reynolds numbers, a representative oscillating frequency is selected. Three mean angles are chosen as the centre of the sinusoidal oscillation in the mean, positive linear, positive, and negative regions of the polars. The combined effects of the Reynolds number and reduced frequency can be isolated, starting with the positive regime. A delay is observed in the angle of attack at which stall occurs, which is inversely proportional to It was only possible to test one reduced frequency for all Reynolds numbers due to setup limitations, corresponding to a value of  $k = 0.091$  as seen in Tab. 3.

The negative region of the polars is shown in Fig. 10 (a), where the Reynolds number. This is due to the higher inertia introduced in the system, at which the reduced frequency decreases and with decreasing free-stream velocity. The normal coefficient magnitude decreases with increasing Reynolds numbers and reduced frequencies to the point where, for highly unsteady reduced frequencies, separation does not take place for angles of attack as high as  $\alpha = 16.6^\circ$ . The linear region of the polars shows minor differences in magnitude. A difference in slope is found as both parameters are varied, in agreement with previous literature (De Tavernier et al., 2021; Kiefer et al., 2022). The linear region slope is found to affect the negative stall behaviour, following the same trend as the positive region of the polars in Fig. 10 (c). The trends align with the static data results, where the lowest Reynolds number corresponds to the highest forces. Unlike Fig. 10 (a), the reattachment behaviour is found to be mostly independent of the Reynolds number for the negative region of the polars.

In the linear region, the Reynolds number barely affects the slope and forces magnitude, with all cases showing similar values in both the nose-up and nose-down motions. The hysteresis loop displays the same difference in nose-up and nose-down behaviour.

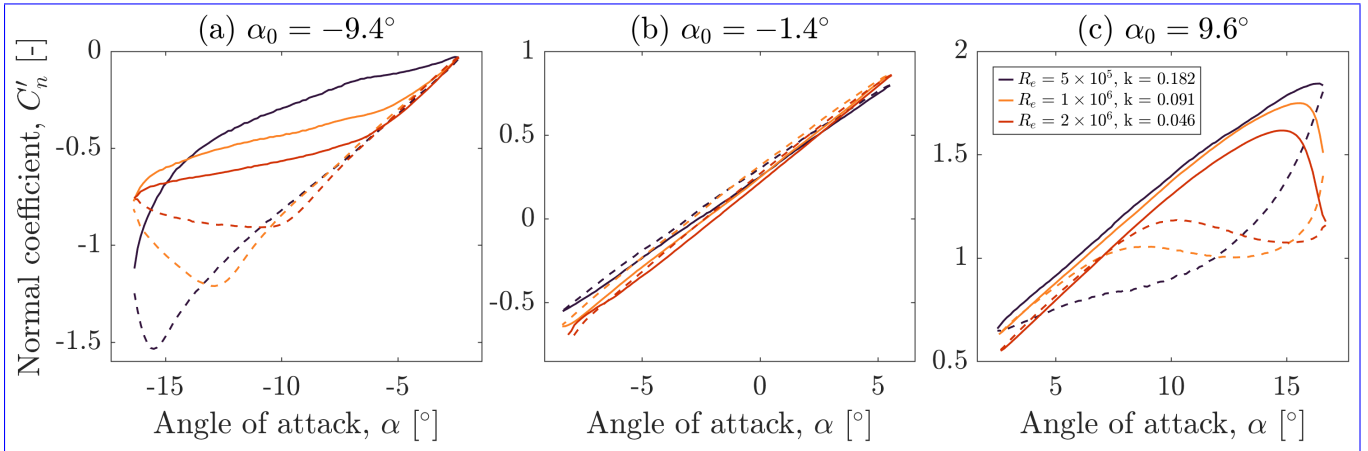


**Figure 11.** Reduced frequencies and Reynolds numbers effects combined for  $f = 1.2Hz$ ,  $A = 7^\circ$ . The reduced frequency range is  $k = 0.182, 0.091, 0.046$ . The full line represents the upstroke airfoil section movement, while the dotted line represents the downstroke movement. Data averaged over 50 dynamic stall cycles.

365 In the positive regime, higher loads are observed for the lowest Reynolds number, in line with the static results shown in figure 9. The flow reattachment behaviour during the nose down motion is found to increase with decreasing reduced frequencies and increasing Reynolds numbers. Lastly, the negative region of the polars showcases two different reattachment regimes. Here, similarly to the positive region, the highest reduced frequencies and Reynolds numbers keep the boundary layer attached at lower angles of attack. At the end of the oscillation, dynamic stall occurs abruptly, leading to a drastic  
 370 increase in normal coefficient and a rapid reattachment mechanism, significantly faster than the equivalent at lower reduced frequencies exhibit significant differences, where for  $Re_c = 5 \times 10^5$  and  $2 \times 10^6$ , the behaviour appears smooth and gradual. For  $Re_c = 10^6$ , strong reattachment is observed in the data, with an accelerated reattachment behaviour as the airfoil oscillates back into the linear region. As for the static case, for the FFA-W3-211 airfoil, dynamic experiments of  $Re_c = 2 \times 10^6$  or above are recommended to better capture the physical trends relevant for larger wind turbine blades.

### 375 **3.3.2 Reduced Combined Reynolds number and reduced frequency effects**

Together with the Reynolds number, the reduced frequency directly affects the airfoil performance. Given the low Mach number, it is possible to isolate combine the effects of  $k$  by varying the oscillating frequency, described in Eq. (4), and Reynolds number. It was only possible to test one reduced frequency for all Reynolds numbers due to setup limitations, corresponding to a value of  $k = 0.091$  as seen in Tab. 3 and marked in red. This value falls in the unsteady regime according to Corke and  
 380 Thomas (2015).

The results are shown in Fig. 10. Except for a decreasing force magnitude in upstroke results for the linear and positive regions, these two seem relatively independent of 11. Firstly, reattachment in the Reynolds number. However, the two regions

**Table 3.** Reduced frequencies range matrix for the dynamic oscillations. It is possible to compare results from different Reynolds numbers for the same value of  $k = 0.091$ .

/	<del><math>Re = 5 \times 10^5</math></del> <u><math>Re_c = 5 \times 10^5</math></u>	<del><math>Re = 10^6</math></del> <u><math>Re_c = 10^6</math></u>	<del><math>Re = 2 \times 10^6</math></del> <u><math>Re_c = 2 \times 10^6</math></u>
$f = 0.6Hz$	<u>0.091</u>	0.046	0.023
$f = 1.2Hz$	0.182	<u>0.091</u>	0.046
$f = 1.8Hz$	0.273	0.137	0.068
$f = 2.4Hz$	0.365	0.182	<u>0.091</u>

show great differences for the same reduced frequency. Firstly, the nose-down reattachment downstroke movement in Fig. 10 (c) exhibits different magnitudes and behaviours as a result of different reduced frequencies. Fig. 10 (a-c) showcased the isolated effects of the Reynolds number, which only affected the dynamic polars in the negative and positive stall and reattachment behaviour. Therefore, the significant stall delay and higher magnitude shown in Fig. 10 (e) exhibits different magnitudes and behaviours. 11 (a-c) can be attributed to changing values of  $k$ .

For the lowest Reynolds number and frequency, the reattachment is quite linear. As both parameters double, the initial reattachment is faster, with a strong and sudden decrease in loads. The last case, for  $Re_c = 2 \times 10^6$  and  $f = 2.4Hz$ , bridges between the two previous cases. Secondly, the In the negative region of the polars shows clear Reynolds numbers effects in the negative stall region. These, the unsteady effects are visible in the lower minimum normal coefficient attained at higher Reynolds numbers. All cases show a smooth negative stall, with no sudden decrease in loads as observed in the positive static region due to the airfoil's camber. Finally, the, where higher reduced frequencies are responsible for larger force differences in the nose-down and nose-up motion in the negative region shows a consistent reattachment trend, which can be considered independent of the Reynolds number and oscillating frequency motions. The mechanisms that describe the boundary layer attachment are a function of the variation in leading-edge suction peak and trailing-edge stall evolution.

This is due to the higher inertia introduced in the system, at which the reduced frequency decreases and with decreasing free-stream velocity. The normal coefficient magnitude decreases with increasing Reynolds numbers and reduced frequencies to the point where, for highly unsteady reduced frequencies, separation does not take place for angles of attack as high as  $\alpha = 16.6^\circ$ .

The linear region of the polars shows minor differences in magnitude. A difference in slope is found as both parameters are varied, in agreement with previous literature (De Tavernier et al., 2021; Kiefer et al., 2022). The linear region slope is found to increase with decreasing reduced frequencies, independently of the Reynolds number, as shown in the previous section of the manuscript.

Lastly, the negative region of the polars showcases two different reattachment regimes. Here, similarly to the positive region, the highest reduced frequencies keep the boundary layer attached at lower angles of attack. At the end of the oscillation, dynamic

stall occurs abruptly, leading to a drastic increase in normal coefficient and a rapid reattachment mechanism, significantly faster than the equivalent at lower reduced frequencies.

### 3.3.3 Reduced Frequency effects

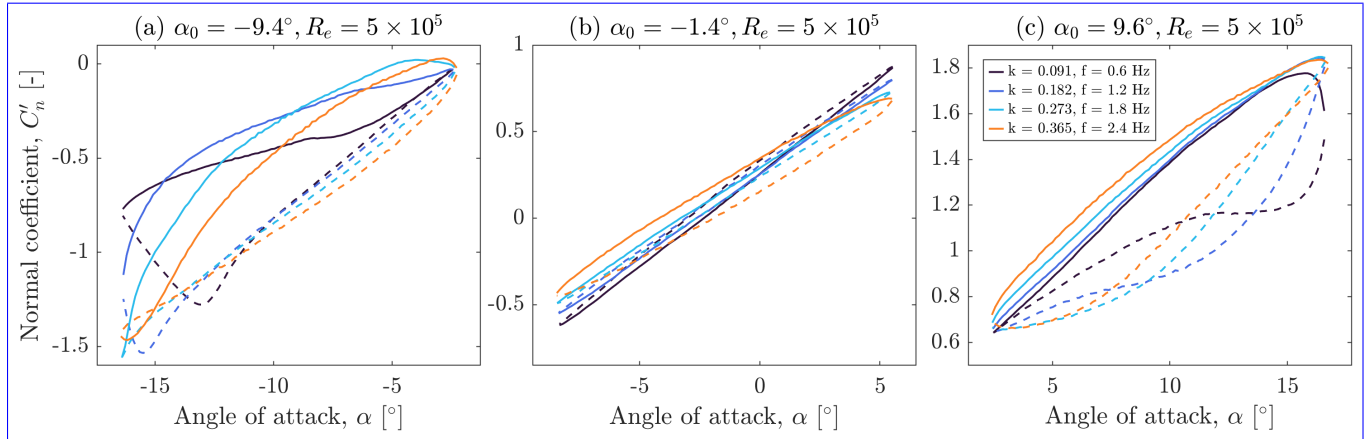


**Figure 12.** Reduced Oscillating frequency trend sweep for a constant value of  $k = 0.091 Re_c = 5 \times 10^5$ ,  $A = 7^\circ$ , covering different Reynolds numbers the quasi-steady, unsteady and oscillating frequencies highly unsteady regimes. The full line represents the upstroke wing movement, while the dotted line represents the downstroke wing movement. Data averaged over 50 dynamic stall cycles.

### 410 3.3.4 Frequency effects

The effects of varying the oscillating frequency are shown in Fig. ??, divided by 12, 13 and 14, divided by the same mean angle and Reynolds number. The lowest frequency displays a significantly faster reattachment behaviour for all cases tested. For the lowest reduced frequency of  $k = 0.23$   $k = 0.023$ , the flow can be considered quasi-steady (Corke and Thomas, 2015), implying that the flow remains attached for slightly more than its static equivalent case. The peak normal coefficient for the positive mean angles is delayed by a few degrees and displays a higher magnitude than the static equivalent, with the value increasing as the frequency increases for all Reynolds numbers. At the highest reduced frequencies, registered for  $Re_c = 5 \times 10^5$ , the difference in maximum normal coefficient decreases as the boundary layer remains attached for longer during the upstroke motion. For  $k = 0.182, 0.273, 0.365$ , no boundary layer separation is observed in the upstroke motion, which reaches  $\alpha = 17.6^\circ$ . The only case to display separation is at  $k = 0.091$ , where dynamic stall is observed at  $\alpha \approx 15^\circ$ .

420 Reattachment behaviour for the mean positive angle shows good consistency within the same Reynolds number sweep. Both  $Re_c = 10^6$  and  $Re_c = 2 \times 10^6$  display the same trend where reattachment is fastest at the lowest reduced frequencies. As the reduced frequency increases, the flow remains detached from the airfoil for longer, leading to a higher loss of normal coefficient. Here, for the highest reduced frequency case, the shape of the hysteresis loop almost resembles the one found in the

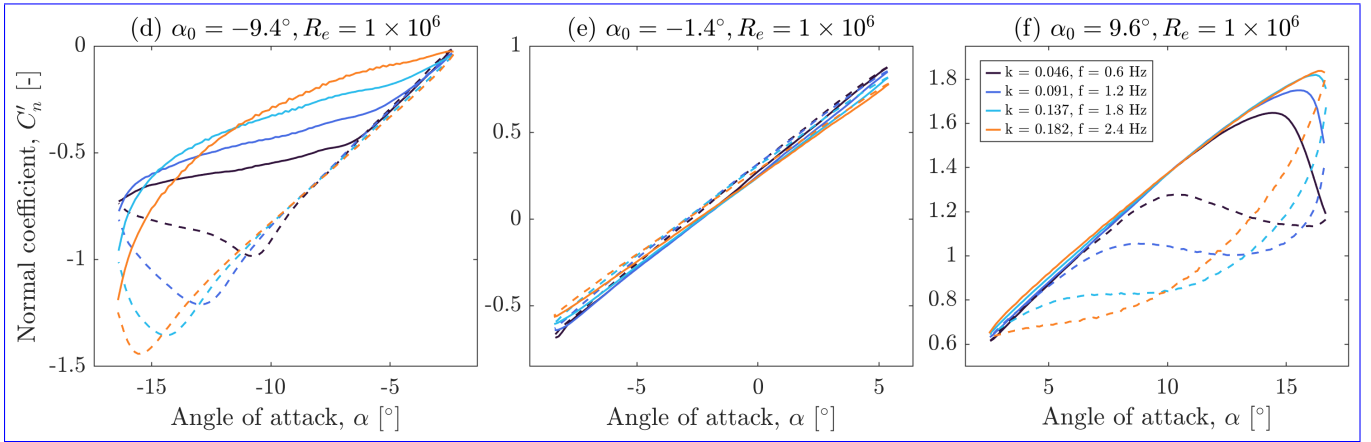


**Figure 13.** Oscillating frequency sweep for  $Re_c = 2 \times 10^6, A = 7^\circ$ ,  $Re_c = 10^6, A = 7^\circ$ , covering the quasi-steady, unsteady and highly unsteady regimes. The full line represents the upstroke wing movement, while the dotted line represents the downstroke wing movement. Data averaged over 50 dynamic stall cycles.

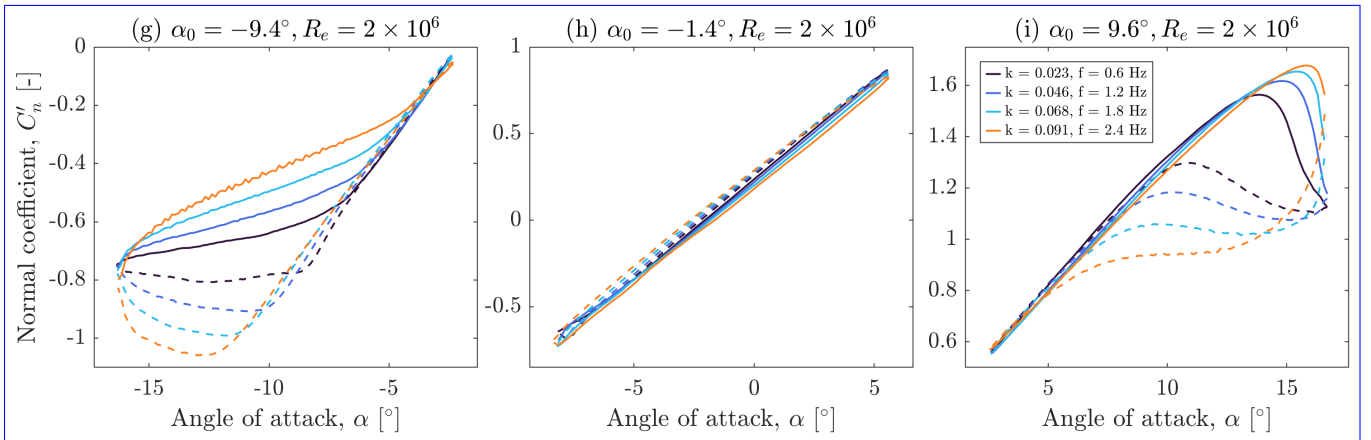


**Figure 14.** Oscillating frequency sweep for  $Re_c = 2 \times 10^6, A = 7^\circ$ , covering the quasi-steady, unsteady and highly unsteady regimes. The full line represents the upstroke wing movement, while the dotted line represents the downstroke wing movement. Data averaged over 50 dynamic stall cycles.

425 linear region, where the upstroke and downstroke motions showcase greatly different force magnitudes. In general, all reduced frequencies do not converge back to the original linear region slope found at the beginning of the upstroke oscillation, unlike other cases shown in Fig. 13 and Fig. 14. Due to the higher reduced frequencies obtained from the same oscillating frequency value combined with a lower free stream, the  $Re_c = 5 \times 10^5$  displays a more unsteady reattachment behaviour.

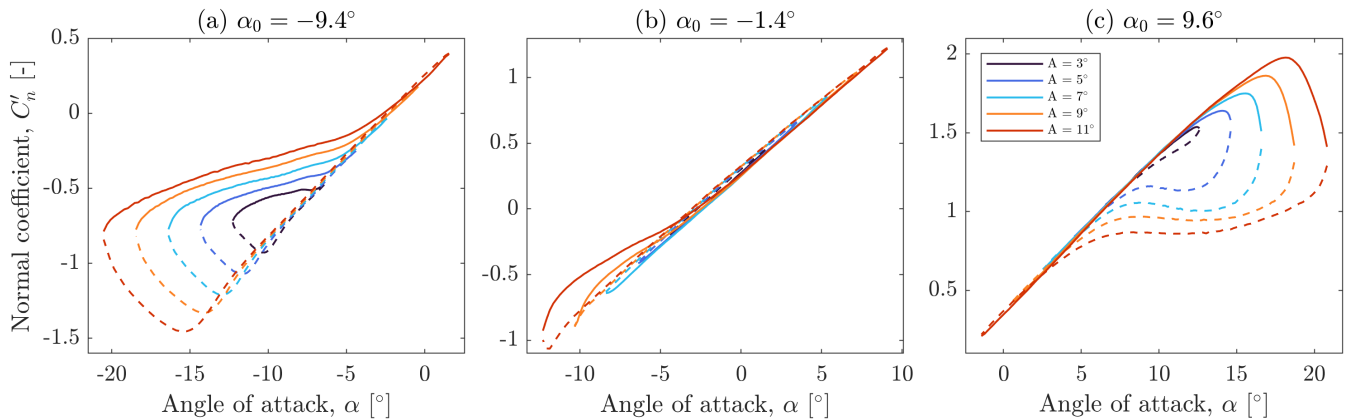


**Figure 15.** Amplitude sweep for  $Re_c = 1 \times 10^6$ ,  $f = 1.2\text{Hz}$ , covering the quasi-steady, unsteady and highly unsteady regimes. The full line represents the upstroke airfoil section movement, while the dotted line represents the downstroke movement. Data averaged over 50 dynamic stall cycles.

Finally, the oscillating frequency is found to influence the linear region slope. ~~The force slope decreases with increasing instability.~~ Here, a Reynolds number dependency is also observed, for which the upstroke and downstroke difference in time-averaged normal coefficient exhibits fewer differences as the Reynolds number increases. Following the conclusions of some high-Reynolds numbers literature (Kiefer et al., 2022), it is expected that the thinner boundary layer will progressively reduce the upstroke and downstroke difference in pressure distribution. ~~Stall is classified as trailing edge, with the separation point fastly moving upstream of the airfoil until the flow is fully detached from the airfoil, depending on the oscillating amplitude. One interesting effect is noted here. Except for one, all the presented linear region cases exhibit a stronger normal coefficient magnitude during the downstroke phase. The only case this does not occur is for the highest tested reduced frequency of  $k = 0.364$ . Here, due to the higher flow instability, the airfoil's upstroke motion shows stronger loads.~~

### 3.3.4 Amplitude effects

Results in Fig. 15 display the effects of the oscillating amplitude for a Reynolds number of  $Re_c = 10^6$ . While pitching the airfoil around the same mean angle, it is immediately visible how, for the positive and negative regions of the polars, the dynamic loop shape is similar between all cases and changes linearly with the angle of attack. For the linear region case, the highest oscillations can already capture the effects of dynamic stall in the lower regime, showing a difference in normal coefficient for the same angle of attack. This is particularly visible for the  $A = 11^\circ$  case, where the oscillation is large enough to capture the dynamic stall loop cycle. As expected, there are differences between the positive and negative regions of the polars due to the airfoil's camber. Due to the cambered nature of the FFA-W3-211 airfoil, a larger dynamic stall loop is associated with the negative region of the polars where the convergence to the linear region is slow and displays greater discrepancies in

the force magnitude. One example is the flow reattachment behaviour, which is observed to be linear in the negative region, while this exhibits a force increase in the positive region.

### 3.4 Dynamic pressure coefficient distribution

Similar to the static counterpart, the dynamic pressure coefficient was retrieved through integration the pressure taps. Given the  
 450 airfoil oscillation, these were averaged for an instantaneous angle of attack with a tolerance of  $\pm 0.1^\circ$ . A number of taps were excluded from the analysis as these were found to be partially blocked, slow or unplugged. As a result, the following plots are obtained from a pressure distribution of 83 pressure taps.

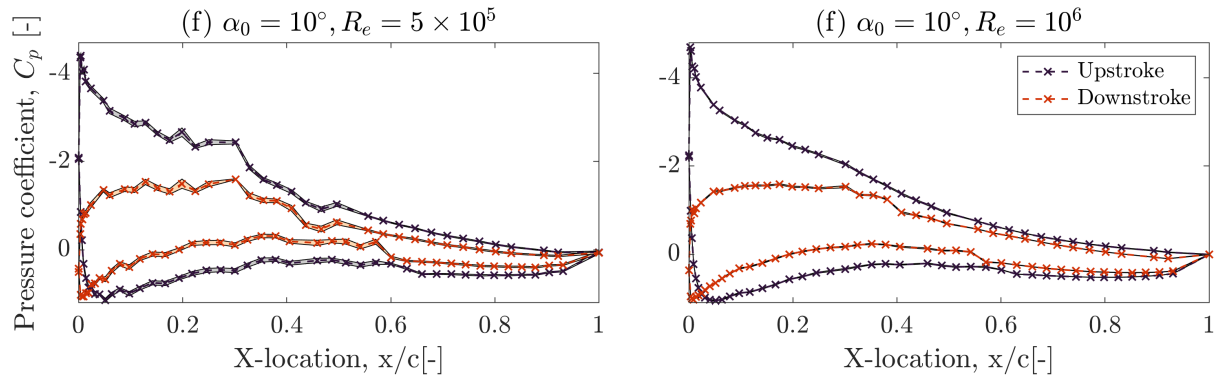


**Figure 16.** Pressure coefficient standard deviation computed for  $A = 7^\circ$ ,  $f = 1.2Hz$

In Fig. 17, results are presented for angle of attack of  $\alpha = -13^\circ$  and  $\alpha = 14^\circ$ . Due to the pressure scanner range, the average pressure distribution exhibits a lower resolution at low Reynolds numbers (see Fig. ??16).

455 ~~As this-~~ As the Reynolds number increases, the data appears smoother, also thanks to the lower reduced frequency. ~~The LSB observed in the static results is present for  $Re = 5 \times 10^5, 10^6$  cases, and its magnitude decreases as the Reynolds number increases. It can also~~ decreasing frequency (Fig. 17). Particularly at the lower Reynolds numbers, the discrepancies in the pressure are significant, making it hard to distinguish a LSB. Here, the pressure distributions hint towards the presence of an  
 460 of  $Re_c = 10^6$ , as shown in Fig. 16. It can be noted that the pressure distribution values are not identical and significantly vary  
vary significantly for the upstroke and downstroke motions, as suggested in previous plots. The negative ~~region of the polars~~  
~~showcases~~ values of pressure distribution showcase a clear suction peak in the downstroke motion, which collapses as the airfoil is pitched up. Similar to the static case, this depends on the Reynolds number and reduced frequency combination, and it collapses as the Reynolds number increases. This is partially mitigated by the reduced frequency term. As the flow reattaches,  
 465 the trailing edge provides the lift, which presents the highest pressure difference. The hysteresis loop is caused by the unsteady flow effects. In the deep dynamic stall conditions, unsteady effects are predominant, with higher force values obtained at higher angles of attack. As highlighted in Kiefer et al. (2022), two mechanisms are responsible for the load development. This

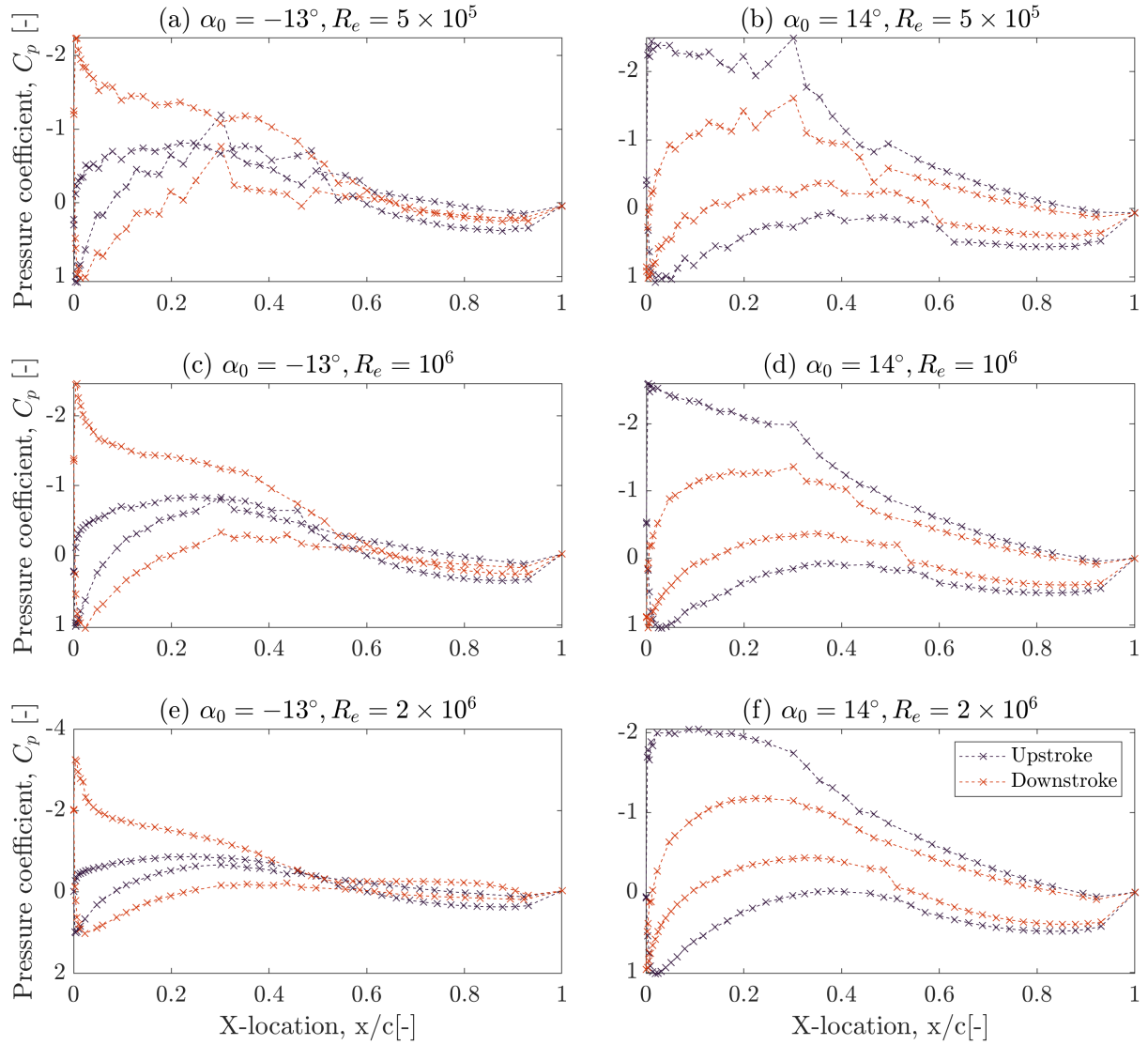


**Figure 17.** Dynamic pressure coefficient for  $A = 7^\circ, f = 1.2Hz$

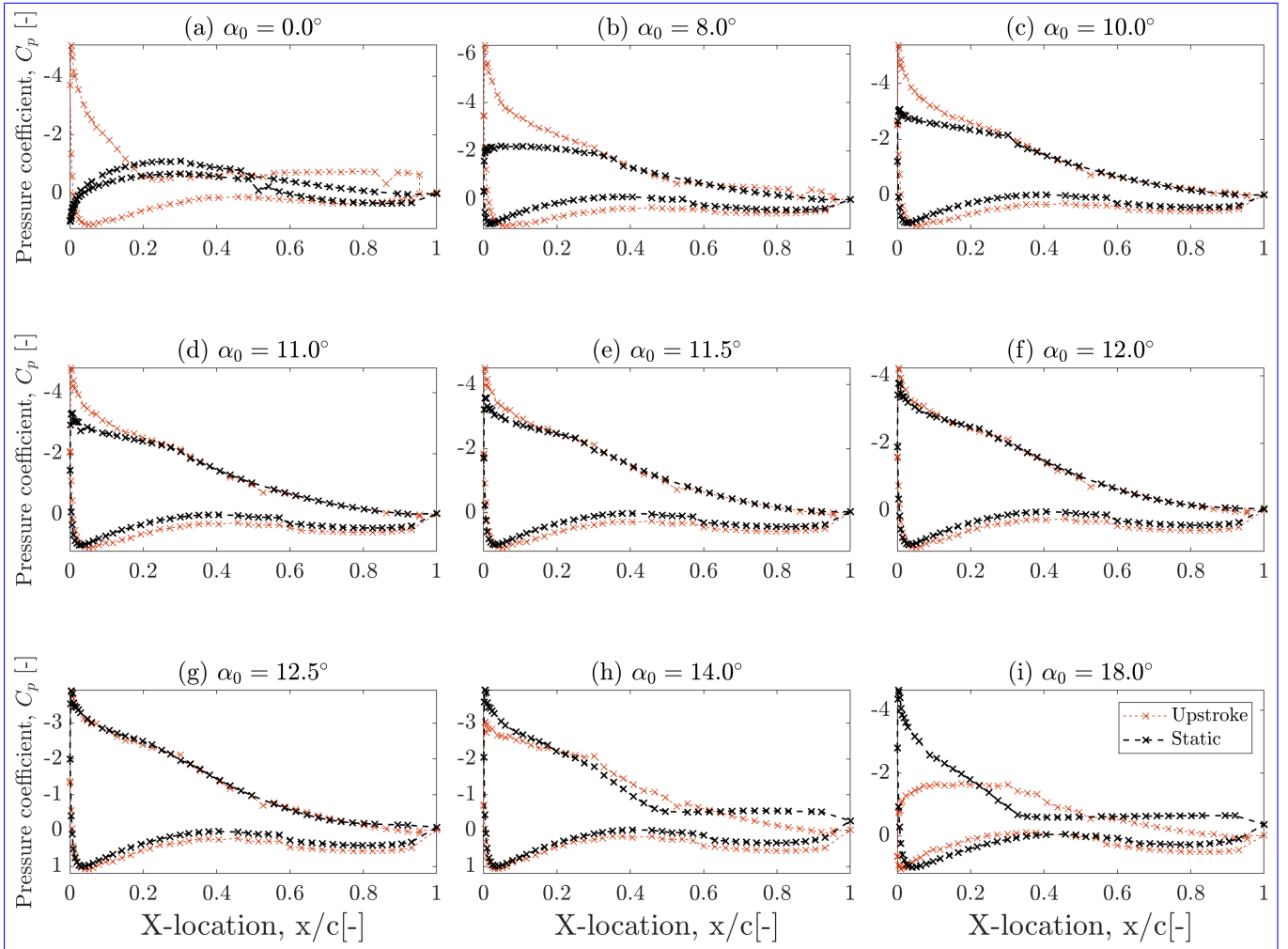


**Figure 18.** Static and dynamic pressure coefficient comparison for positive angles,  $Re_c = 10^6$ ,  $f = 1.2Hz$ . At  $\alpha = 18^\circ$ , the trailing edge still displays attached flow during the upstroke oscillation.

is driven by the increase in suction peak magnitude near the leading edge and the boundary layer separation mechanisms originating at the trailing edge. The magnitude variation of the suction peak is responsible for the lift increase. In Fig. 18, a comparison between the static and dynamic pressure distribution is drawn for the same Reynolds number. It can be readily noted that, for  $\alpha = 14^\circ$ , the static data shows a stalled trailing edge, while the upstroke dynamic data still showcases an attached flow behaviour. This is followed by abrupt dynamic stall at  $\alpha = 18^\circ$ , where the dynamic suction peak collapses. Overall, the pressure distribution results show good agreement around the static stall region, despite the higher dynamic suction peak for the pre-stall angles of attack.

#### 475 4 Conclusions

This work describes the experimental aerodynamic characterisation of the FFA-W3-211 airfoil. The wind energy community widely uses ~~the this~~ airfoil as a popular reference. An experiment was performed in the low-speed, low-turbulence wind tunnel at ~~the~~ Delft University of Technology, for which a new airfoil section model with a chord length of  ~~$e = 600\text{m}$~~   $c = 600\text{mm}$  and height of  $h = 1246\text{mm}$  was manufactured. Previously, several wing geometries have been tested in this facility. The airfoil section was pitched sinusoidally in time around its ~~quarter-chord point~~ quarter-chord line to acquire the first dynamic data for the airfoil geometry for chord-based Reynolds numbers of up to  $Re_c = 2 \times 10^6$ .

The static data ~~highlight suggest~~ the presence of a laminar separation bubble that disappears with increasing Reynolds numbers. ~~This flow feature is~~ Such a flow feature could be responsible for the ~~shift in~~ observed shift in maximum lift trends and static stall behaviour. ~~Similar to the collapse of the LSB, the suction peak magnitude and separation point exhibit strong dependencies on the Reynolds number.~~

observed around  $Re_c = 2 \times 10^6$ . The dynamic results display the effects of ~~the individual variation of~~ individual variations in inflow and oscillating parameters. The reduced frequency and Reynolds number effects were described, highlighting their influence on dynamic stall, reattachment and hysteresis loops. For increasing amplitudes, the shape of the hysteresis loop was maintained, but the magnitude increased. This allows for a simple empirical model to capture this effect. The upstroke and downstroke pressure distributions showcase fundamental differences in ~~flow structure~~ flow structure development, ultimately affecting the overall force balance.

From the findings reported here, it is recommended to use experimental data of  $Re_c = 2 \times 10^6$  or above in simulations and model validation or tuning to capture the correct physical (static and dynamic) trends of the FFA-W3-211 airfoil relevant for larger wind turbine blades. For dynamic stall model tuning, it may also be important to consider the significant change in behavior between positive and negative stall angles. Experiments at higher Reynolds numbers than possible for this study would be highly valuable to confirm whether the  $Re_c = 2 \times 10^6$  threshold is sufficient. It is also important to bear in mind that the airfoil shape and roughness also plays an important role.

*Data availability.* Data can be downloaded under CC BY 4.0 license at 10.4121/92716ecf-b075-41a1-ab93-8e2af785a404

## Appendix A

500 An initial shift of  $\alpha = 1.4^\circ$  was observed in the dynamic data. As a result, a calibration was carried out against both static and dynamic ultra-low frequency data. This has allowed to quantify the shift, which is consistent for most cases for  $Re = 5 \times 10^5, 10^6$  and the negative mean angles for  $Re = 2 \times 10^6$ . However, in some occasions, the data shift observed in the positive regime for the highest Reynolds number shows some irregularities which fall in the  $\pm 1^\circ$  regime. This has to be assumed as the reported experimental error for the pitching airfoil cases.

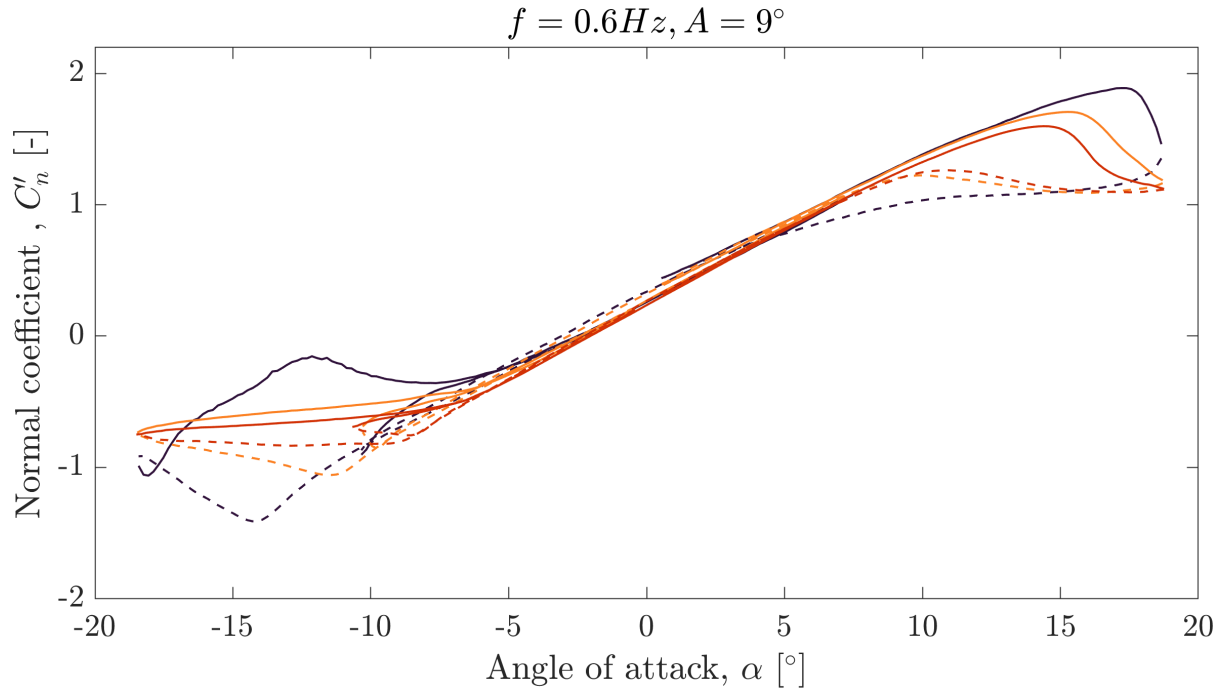


**Figure A1.** Data overlap between the negative, mean and positive regimes for  $A = 9^\circ$ ,  $f = 0.6 Hz$ .

505 *Author contributions.* SC was responsible for the overall research, under the supervision of DDT and DvT. SC carried out the experimental measurements as well as the post-processing, visualization and analysis of the measurements.

*Competing interests.* The authors declare that they have no conflict of interest.

## References

- Baldacchino, D., Ferreira, C., Tavernier, D. D., Timmer, W., and Van Bussel, G.: Experimental parameter study for passive vortex generators on a 30% thick airfoil, *Wind Energy*, 21, 745–765, 2018.
- Bergh, H. and Tijdeman, H.: Theoretical and experimental results for the dynamic response of pressure measuring systems, 1965.
- Bertagnolio, F., Sørensen, N., Johansen, J., and Fuglsang, P.: Wind turbine airfoil catalogue, 2001.
- Boutet, J., Dimitriadis, G., and Amandolese, X.: A modified Leishman–Beddoes model for airfoil sections undergoing dynamic stall at low Reynolds numbers, *Journal of Fluids and Structures*, 93, 102 852, 2020.
- Boye, T. and Xie, Z.-T.: Aerodynamics of a pitching wind turbine blade at high reduced frequencies, *Journal of Wind Engineering and Industrial Aerodynamics*, 223, 104 935, 2022.
- Brunner, C. E., Kiefer, J., Hansen, M. O., and Hultmark, M.: Study of Reynolds number effects on the aerodynamics of a moderately thick airfoil using a high-pressure wind tunnel, *Experiments in Fluids*, 62, 1–17, 2021.
- Carta, F. O.: Analysis of oscillatory pressure data including dynamic stall effects, Tech. rep., NASA, 1974.
- Ceyhan, J. S. O., Boorsma, K., Gonzalez, A., Munduate, X., Pires, O., Sørensen, N., Ferreira, C., Sieros, G., Madsen, J., Voutsinas, S., et al.: Latest results from the EU project AVATAR: Aerodynamic modelling of 10 MW wind turbines, in: *Journal of Physics: Conference Series*, vol. 753, p. 022017, IOP Publishing, 2016.
- Ceyhan, O., Pires, O., Munduate, X., Sorensen, N. N., Schaffarczyk, A. P., Reichstein, T., Diakakis, K., Papadakis, G., Daniele, E., Schwarz, M., et al.: Summary of the blind test campaign to predict the high Reynolds number performance of DU00-W-210 airfoil, in: *35th Wind Energy Symposium*, p. 0915, 2017.
- Chellini, S., De Tavenier, D., and Von Terzi, D.: Impact of dynamic stall model tailoring on wind turbine loads and performance prediction, in: *Journal of Physics: Conference Series*, vol. 2767, p. 022016, IOP Publishing, 2024.
- Choudhuri, P. G. and Knight, D.: Effects of compressibility, pitch rate, and Reynolds number on unsteady incipient leading-edge boundary layer separation over a pitching airfoil, *Journal of Fluid Mechanics*, 308, 195–217, 1996.
- Corke, T. C. and Thomas, F. O.: Dynamic stall in pitching airfoils: aerodynamic damping and compressibility effects, *Annual Review of Fluid Mechanics*, 47, 479–505, 2015.
- Dalton, C.: Allen and Vincenti blockage corrections in a wind tunnel, *AIAA Journal*, 9, 1864–1865, 1971.
- De Tavernier, D., Ferreira, C., Viré, A., LeBlanc, B., and Bernardy, S.: Controlling dynamic stall using vortex generators on a wind turbine airfoil, *Renewable Energy*, 172, 1194–1211, 2021.
- Delft: Low turbulence tunnel, <https://www.tudelft.nl>, accessed: 18/09/2023, 2017.
- Gaertner, E., Rinker, J., Sethuraman, L., Zahle, F., Anderson, B., Barter, G., Abbas, N., Meng, F., Bortolotti, P., Skrzypinski, W., et al.: Definition of the IEA 15-megawatt offshore reference wind turbine, 2020.
- Gardner, A. D., Jones, A. R., Mulleners, K., Naughton, J. W., and Smith, M. J.: Review of rotating wing dynamic stall: Experiments and flow control, *Progress in Aerospace Sciences*, 137, 100 887, 2023.
- Gharali, K. and Johnson, D. A.: Dynamic stall simulation of a pitching airfoil under unsteady freestream velocity, *Journal of Fluids and Structures*, 42, 228–244, 2013.
- Ham, N. D.: Stall flutter of helicopter rotor blades: a special case of the dynamic stall phenomenon, *Journal of the American Helicopter Society*, 12, 19–21, 1967.

- Kiefer, J., Brunner, C. E., Hansen, M. O., and Hultmark, M.: Dynamic stall at high Reynolds numbers induced by ramp-type pitching motions, *Journal of Fluid Mechanics*, 938, A10, 2022.
- 545 Leishman, J.: Dynamic stall experiments on the NACA 23012 aerofoil, *Experiments in Fluids*, 9, 49–58, 1990.
- Leishman, J. G.: Challenges in modelling the unsteady aerodynamics of wind turbines, *Wind Energy: An International Journal for Progress and Applications in Wind Power Conversion Technology*, 5, 85–132, 2002.
- Leishman, J. G. and Beddoes, T.: A Semi-Empirical model for dynamic stall, *Journal of the American Helicopter society*, 34, 3–17, 1989.
- 550 Llorente, E., Gorostidi, A., Jacobs, M., Timmer, W., Mundaate, X., and Pires, O.: Wind tunnel tests of wind turbine airfoils at high Reynolds numbers, in: *Journal of Physics: Conference Series*, vol. 524, p. 012012, IOP Publishing, 2014.
- McAlister, K. W., Carr, L. W., and McCroskey, W. J.: Dynamic stall experiments on the NACA 0012 airfoil, Tech. rep., 1978.
- McAlister, K. W., Lambert, O., and Petot, D.: Application of the ONERA model of dynamic stall, Tech. rep., 1984.
- McCroskey, W. J.: *Unsteady airfoils*, 1982.
- 555 Melani, P., Aryan, N., Greco, L., and Bianchini, A.: The Beddoes-Leishman dynamic stall model: Critical aspects in implementation and calibration, *Renewable and Sustainable Energy Reviews*, 202, 114677, 2024.
- Øye, S.: Dynamic stall simulated as time lag of separation, in: *Proceedings of the 4th IEA Symposium on the Aerodynamics of Wind Turbines*, vol. 27, p. 28, Rome, Italy, 1991.
- Patterson, M. and Lorber, P.: Computational and experimental studies of compressible dynamic stall, *Journal of fluids and structures*, 4, 259–285, 1990.
- 560 Rainbird, J. M., Bianchini, A., Balduzzi, F., Peiró, J., Graham, J. M. R., Ferrara, G., and Ferrari, L.: On the influence of virtual camber effect on airfoil polars for use in simulations of Darrieus wind turbines, *Energy Conversion and Management*, 106, 373–384, 2015.
- Snel, H.: Heuristic modelling of dynamic stall characteristics, in: *EWEC-conference-*, pp. 429–433, Bookshop for Scientific Publications, 1997.
- 565 Stettner, M., Reijerkerk, M. J., L<sup>o</sup>nenschlo<sup>u</sup>, A., Riziotis, V., Croce, A., Sartori, L., Riva, R., and Peeringa, J. M.: Stall-Induced Vibrations of the AVATAR Rotor Blade, *Journal of Physics: Conference Series*, 753, 042019, <https://doi.org/10.1088/1742-6596/753/4/042019>, 2016.
- Timmer, W. and Van Rooij, R.: Summary of the Delft University wind turbine dedicated airfoils, *J. Sol. Energy Eng.*, 125, 488–496, 2003.
- Tuncer, I. H., Wu, J. C., and Wang, C.: Theoretical and numerical studies of oscillating airfoils, *AIAA journal*, 28, 1615–1624, 1990.
- Van Rooij, R.: Modification of the boundary layer calculation in RFOIL for improved airfoil stall prediction, 1996.
- 570 Zahle, F., Barlas, T., Lonbaek, K., Bortolotti, P., Zalkind, D., Wang, L., Labuschagne, C., Sethuraman, L., and Barter, G.: Definition of the IEA wind 22-megawatt offshore reference wind turbine, Tech. rep., National Renewable Energy Laboratory (NREL), Golden, CO (United States), 2024.